THE ASTROPHYSICAL JOURNAL, 383:645–663, 1991 December 20

INFRARED DUST AND MILLIMETER-WAVE CARBON MONOXIDE EMISSION IN THE ORION REGION

JOHN BALLY AND WILLIAM D. LANGER[1]
HOH L245, AT&T Bell Laboratories, Crawford Hill, Holmdel-Keyport Road, Holmdel, NJ 07733

AND

WEIHONG LIU[2]
Harvard-Smithsonian Center for Astrophysics, 60 Garden Street, Cambridge, MA 02138
Received 1991 April 1; accepted 1991 June 26

ABSTRACT

We analyze the far-infrared dust emission seen by the *IRAS* satellite in the Orion region as a function of the local radiation field intensity and compare the dust temperature and opacity with ^{12}CO and ^{13}CO emission. We interpret the infrared radiation in the framework of a single component large grain model and a multicomponent grain model consisting of subpopulations of grains with size-dependent temperatures.

We find a strong dependence of the 100 μm optical depth derived using the large grain model on the average line-of-sight dust temperature and radiation field. In the hot environment surrounding high-luminosity sources and H II regions, all dust along the line-of-sight radiates at 100 μm, and the dust-to-gas ratio, based on the 100 μm opacity and $I(^{13}CO)$, appears to be in agreement with the standard value, about 1% by mass. However, in cold regions of the molecular cloud, which comprise over 90% of the projected area on the sky, only a few percent of the total dust is detectable by *IRAS*. The dust-to-gas ratio, based on the 100 μm intensity and the grain temperature derived from the 60–100 μm intensity ratio using a large grain model, is an order of magnitude or more below that found in the hot regions. The large grain model leads to an overestimate of the temperature of most of the dust in a cold cloud, which results in a severe underestimate of the total dust column density. We find a relationship between the inferred dust-to-gas ratio and the radiation field intensity responsible for heating the dust which can be used to estimate the gas column density from the dust opacity derived from the 60 and 100 μm *IRAS* fluxes.

A multicomponent grain model is required to interpret 60 and 100 μm data when small warm grains make a major contribution to the 60 μm intensity. We attempted to use the 12 μm intensity as a measure of the contribution of small stochastically heated warm grains to the longer wavelength infrared flux. With this model the spatial structure of the resulting column density distribution is nonphysical; the column density increases toward the cloud exterior. This behavior may be due to errors in the zero point offset in the infrared intensity distributions, changes in small grain abundance, and variations in the radiation field intensity. The computed dust optical depth is extremely sensitive to small changes in grain temperature. Submillimeter wavelength observations directly sensitive to the large grain emission are required to study the dust column density in most molecular clouds.

In cold regions, there is an inverse correlation between the peak ^{12}CO temperature and the dust temperature. We find that the dust opacity correlates better with peak ^{12}CO temperature than with $I(^{13}CO)$. These results may be explained by small stochastically heated grains dominating even the 100 μm flux in the irradiated surface layers of the cloud.

Subject headings: infrared: sources — interstellar: grains — interstellar: molecules — nebulae: individual (Orion A, Orion B)

1. INTRODUCTION

The composition and physical characteristics of interstellar clouds are studied primarily by observations of radio and infrared emission. While atomic hydrogen is traced directly by the 21 cm line of H I, molecular hydrogen is indirectly probed by rotational transitions of CO, and the dust is traced by its far-infrared and submillimeter continuum radiation. Detailed studies of gas and grain properties of molecular cloud complexes have become possible with the availability of extensive maps of CO and infrared emission on an arcminute scale. Early studies (see references in Boulanger & Perault 1988) emphasized the comparison of 60 and 100 μm emission with 21 cm H I and 2.6 mm ^{12}CO emission. Later work correlated the dust opacity calculated using simplified models of grain emission with the integrated CO line intensity and extended these relationships to ^{13}CO and even $C^{18}O$ (Beichman et al. 1988; Langer et al. 1989).

Changes in the intensity of the interstellar radiation field alter the heating of the gas and grains which result in variations in the derived relationships between gas and dust tracers. Langer et al. (1989) studied B5, a small molecular cloud exposed primarily to the average interstellar radiation field and containing only low-luminosity and low-mass embedded stars. They found a correlation between 100 μm opacity (derived from the 60 and 100 μm data) and the ^{13}CO column

[1] Postal address: MS 169-327, Jet Propulsion Laboratory, Pasadena, CA 91109.
[2] Also New York University.

density which is significantly better than that using the 100 μm intensity and/or ^{12}CO intensity. However, near the embedded sources in B5, these relationships deteriorate. Further evidence of the importance of variations in the radiation field was found in the comparison of 12 and 25 μm emission with CO which show that the shorter wavelength infrared flux is produced in the cloud envelope where the UV radiation is stronger and small grain stochastic heating dominates (Beichman et al. 1988). Boulanger et al. (1988) studied the gas and dust in the high-luminosity California nebula region, finding correlations between gas and dust tracers which are different from those in B5 and which also imply a dependence on the local radiation environment.

The Orion molecular cloud complex is an active region of star formation in which are found a large variety of physical conditions and radiation field environments. While some portions of the complex have conditions similar to dark clouds with no embedded or nearby sources, most other regions contain embedded or nearby stars ranging from low-mass, low-luminosity objects to massive O stars whose luminosity can produce radiation fields 10^5 times greater than the average value in the local interstellar medium. The Orion region provides an opportunity to investigate the effects of large variations in the radiation environment on the dust and gas. The entire complex lies between 380 and 500 pc from the Sun and about 10°–20° below the Galactic plane where confusion from unrelated background or foreground objects is reduced.

In this paper we study the relationships between grain and gas properties in the Orion region using the *Infrared Astronomy Satellite* (*IRAS*) survey at 100, 60, 25, and 12 μm and the AT&T Bell Laboratories ^{12}CO and ^{13}CO surveys with the 7 m antenna. The resolution of these data sets is comparable (about 100″) and about 300,000 millimeter-wave spectra are available covering 50 deg^2 of the sky. We compare the dust and gas emission as a function of the embedded and nearby stellar luminosity and type of star formation. We analyze the data using a large grain model (LGM) as well as a two component model (multicomponent grain model, MCGM) presented by Boulanger et al. (1988). The results from the Orion region can be applied to the problem of interpreting IR emission throughout the Galaxy and in external galaxies.

2. THE ORION REGION

2.1. *IRAS IR Emission*

The *IRAS* survey at 12, 25, 60, and 100 μm provides large-scale maps of infrared emission from interstellar dust (Beichman et al. 1986). It contains a wealth of information about star formation activity, the spatial distribution and column density of dust, and the strength of the radiation field. In order to maximize the angular resolution of the data used for this analysis, *IRAS* co-added 60 and 100 μm images are used to derive the dust temperature and the 100 μm opacity. The co-adds have an angular resolution of about 1′–2′ and a factor of 3 better sensitivity than the Skyflux images. Recent measurements with the *COBE* satellite indicate that the *IRAS* 100 and 60 μm fluxes for extended sources may be in error by as much as a factor of 2 (C. A. Beichman 1990, private communication).

The co-add processing algorithm generates artifacts in the images when bright sources are present in the field of view. The background flux levels are artificially depressed along the satellite scan direction resulting in stripes in the images when bright sources are present. Although the flux levels of bright sources are not effected, as judged by comparison with the Skyflux images, the emission from fainter regions along the stripes can be substantially underestimated. Therefore, our analysis of the vicinity of H II regions is confined to the high-flux regions and to portions of the images away from the stripe artifacts. In Orion the stripes are mostly oriented in a north-south direction. Figure 1*a* shows a global view of the entire Orion region at 100 μm along with the outline of the region we have mapped in ^{13}CO.

2.2. CO $J = 1$–0 *Emission*

The Orion region has been mapped with the AT&T Bell Laboratories 7 m antenna which has a 100″ beam at 110 GHz. We have obtained about 180,000 ^{13}CO spectra, 110,000 ^{12}CO spectra, and several thousand C^{18}O spectra in the $J = 1 \rightarrow 0$ transition, and 20,000 CS $J = 2 \rightarrow 1$ spectra. The ^{13}CO spectra probe cloud internal structure better than ^{12}CO due to its lower abundance and opacity, and the CS lines probe high-density ($n > 10^4$ cm^{-3}) regions. Maps have been presented in a number of papers or reviews (Bally et al. 1987a; Bally 1989, 1990). Details of the observing strategy and calibration can be found in Bally et al. (1987b). The CO and CS data were obtained on a 1′ grid with a velocity resolution of 100 kHz. Some CO $J = 2$–1 data is available in the northern part of the Orion A cloud (Castets et al. 1990). As noted by Bally et al. (1987a; Bally 1990), the Orion clouds consist of filaments, bubbles, and sheets which may be formed by the combined effects of energy injection from stars, magnetic fields, and gravity. The *IRAS* images show that even outside of the CO clouds, the dust consists of filaments and large-scale bubbles. Figure 1*b* shows a global view of the ^{13}CO emission of the major molecular clouds in Orion (see also Fig. 1*c* [Pl. 12]). In general, the brightest regions in the *IRAS* image correspond to the regions of most intense ^{13}CO emission and where the most luminous star-forming regions are located.

3. RESULTS

To calculate the dust temperature and column density we need a model of the dust grain emission. In the past, it has often been assumed that only one large grain size contributes to the emission at any particular wavelength. However, this model is wrong when large grain temperatures are low (less than 25 K—Puget, Leger, & Boulanger 1985) due to the contribution of stochastically heated small grains in low-radiation fields (Draine & Anderson 1985). It can be seen in Boulanger et al.'s (1988) models, which combine both large and small grain emission, that for a given ratio of 60–100 μm flux, there are two possible values for the temperature of the large grains for large grain temperatures below 40 K. In principle, the 12–60 μm ratio can be used to discriminate between the high- and low-temperature branches of their large grain dust temperature solution. Over most of Orion the 12 μm fluxes indicate that the lower branch solution is a better approximation to the large grain temperature. As discussed below, comparison with the ^{13}CO emission shows that the 60–100 μm ratio in either the large grain model, or equivalently, use of the upper branch of the Boulanger et al. model, overestimates the large grain temperature, which leads to a severe underestimate of the 100 μm large grain optical depth in cold regions of molecular clouds. However, according to Figure 4 in Boulanger et al. (1988), use of the 60 and 100 μm flux ratio provides a reasonable value for the large grain temperature above 25 K.

PLATE 12

FIG. 1*c*.—Large-scale view of the Orion region in ^{13}CO integrated intensity covering the velocity range $V_{LSR} = -2$ to 13 km s^{-1}. Coordinates are centered on Orion A.

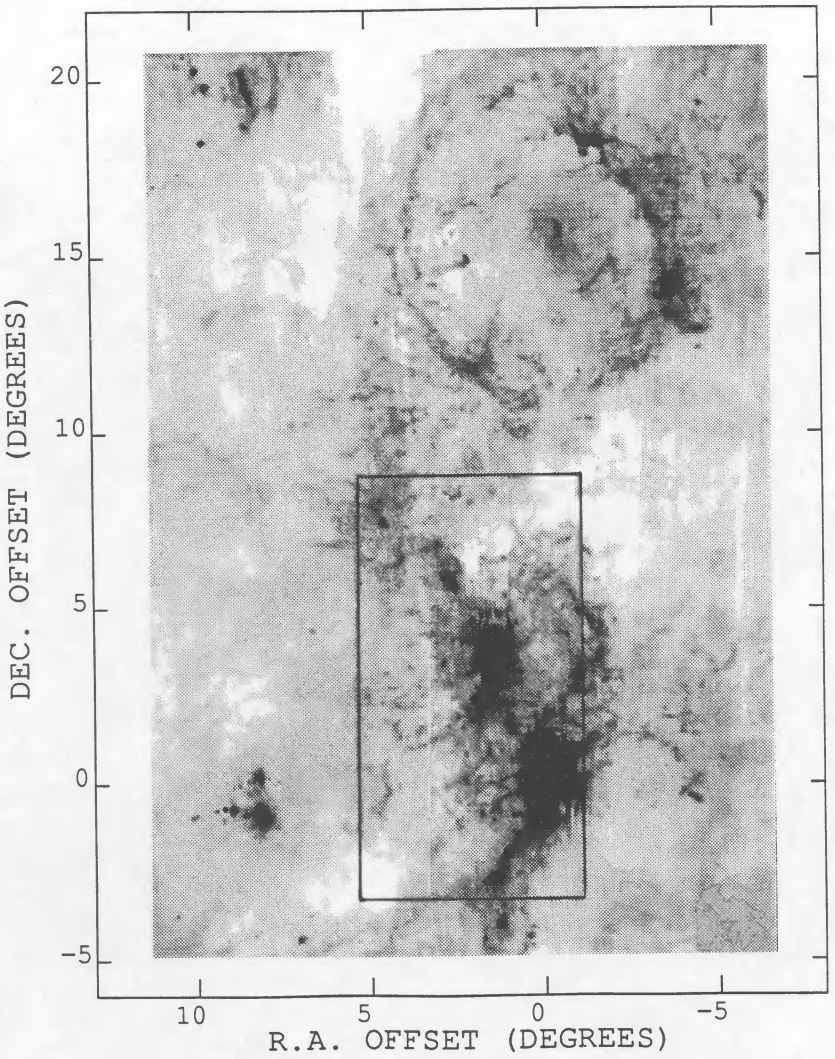

FIG. 1*a*

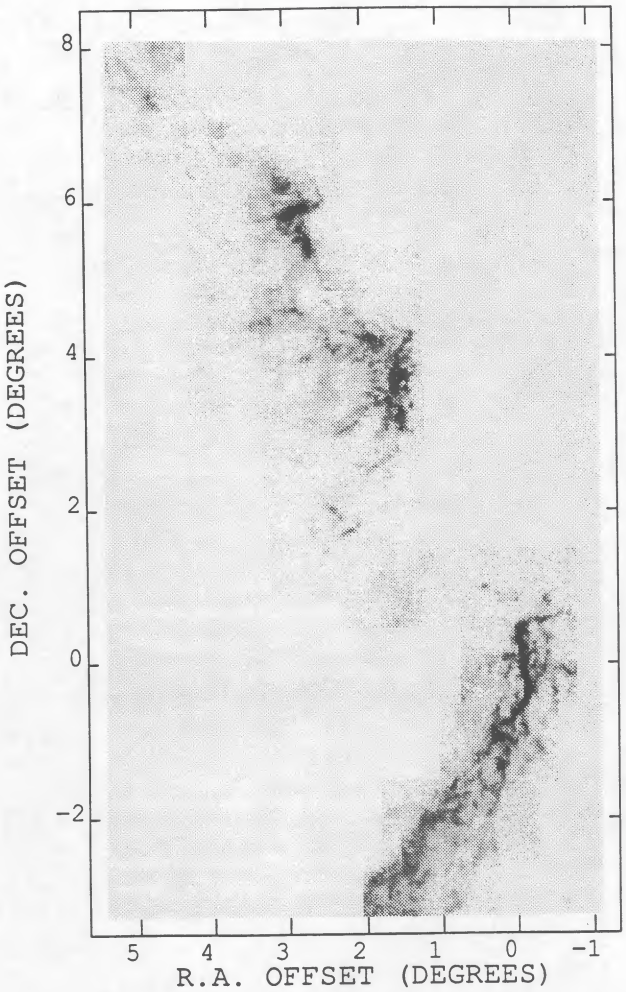

FIG. 1*b*

FIG. 1.—(*a*) Large-scale view of Orion at 100 μm the *IRAS* Skyflux image. Rectangular area marks the boundary of the ^{13}CO image shown in (*b*). Large circular feature at the top is the λ-Ori ring. Orion A is the bright region centered at (0, 0) on the image which corresponds to the coordinates, $\alpha(1950) = 05^{h}32^{m}47^{s}$, $\delta(1950) = -5°24'30''$. Orion B is located about 1°.5 east and 3°.5 north of (0, 0). Mon R2 is located near the bottom left about 7° east and 1° south of Orion A. NGC 2071 and NGC 2068 are contained in the small bright area 2°.5 east and 6° north of (0, 0). (*b*) Large-scale view of the Orion region in ^{13}CO integrated intensity covering the velocity range $V_{LSR} = -2$ to 13 km s^{-1}. Coordinates are centered on Orion A. See also Fig. 1*c* (Plate 12).

TABLE 1

COORDINATES AND BOX DIMENSIONS OF ORION REGIONS

Region	α(1950)	δ(1950)	Area $d\alpha$(arcmin) × $d\delta$(arcmin)
L1641 No. 1	$5^h34^m00^s$	−7°30′00″	20 × 20
L1641 No. 2	5 35 53	−7 04 06	25 × 20
Haro 4-255	5 36 56	−7 28 05	10 × 10
NGC 1999	5 33 57	−6 45 00	15 × 15
NGC 2071	5 44 31	00 20 41	15 × 15
NGC 2068	5 44 12	00 08 00	10 × 10
NGC 2023	5 39 07	−2 17 20	10 × 10
NGC 2024	5 39 12	−1 55 42	15 × 15
Mon R2.....	6 05 22	−6 22 25	15 × 15
M 42	5 32 47	−5 24 30	20 × 20

Unless otherwise stated in this paper, the 100 μm dust optical depth, τ(100 μm) or 100 μm LGM opacity, refers to a quantity calculated from the *IRAS* data within the context of a large grain model. This estimated opacity is much smaller than the actual absorption or emission optical depth, implying that the *IRAS* emission is not sensitive to most of the dust in these regions. References to the true opacity and dust column density will be noted explicitly.

Primarily we analyze the Orion data using a large grain model (equivalent to assuming that we are on the high-temperature branch of the dust temperature curve in a multi-component grain model—see the Appendix). In the large grain model, we use the method described by Langer et al. (1989) to compute the dust opacity and temperature for the Orion region. We also use the multicomponent grain model in which the 12 μm flux images determine where small grain emission dominates the 60 μm (and possibly the 100 μm) emission. This method is described in the Appendix.

The co-adds and the ^{13}CO data each contain about a quarter million points and include regions having very different physical properties. The display of all these data points in a single plot is difficult to interpret, and therefore we restrict detailed analysis to selected subsets of this data in which the dust and gas are exposed to specific (and different) levels of radiation. The regions we have studied range from cold clouds with no known or little star formation activity, to H II regions containing massive and luminous embedded star clusters. The fields of view used for the detailed studies are listed in Table 1. Figure 2*a* (see also Fig. 2*b* [Pl. 13]) consists of a representative sample of the co-added images of dust opacity and temperature, ^{12}CO temperature, and ^{13}CO integrated intensity using the single component LGM. These quantities exhibit complex behavior in the images and will be discussed below and in § 4.

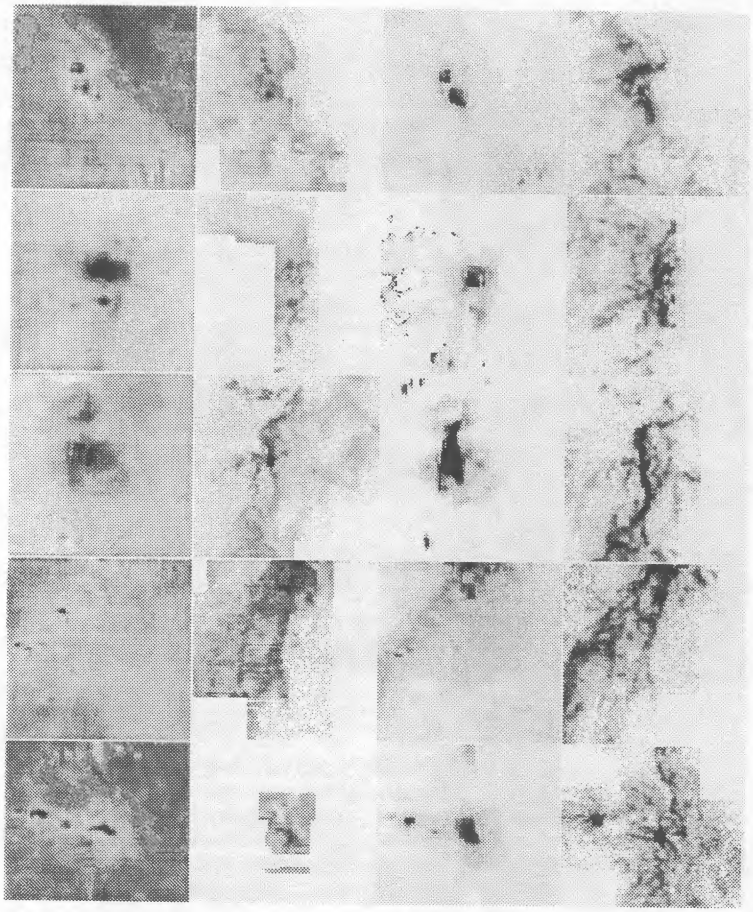

FIG. 2*a*.—Mosaic of images showing five 2°.25 × 2°.25 areas using the *IRAS* co-adds and the AT&T Bell Laboratories 7 m data for NGC 2071 and NGC 2068 (*top row*); Orion B including NGC 2024 and NGC 2023 (*second row*); Orion A including M42 and NGC 1977 (*third row*); L1641 (*fourth row*); and Mon R2 (*bottom row*). Quantities shown in each column are (*from left to right*): 60 μm/100 μm dust color temperature (20–200 K), peak ^{12}CO temperature (0–80 K), 100 μm optical depth in the large grain model (10^{-5} to 10^{-3}), and $I(^{13}\mathrm{CO})$ (0–55 K km s^{-1}). See also Fig. 2*b* (Plate 13).

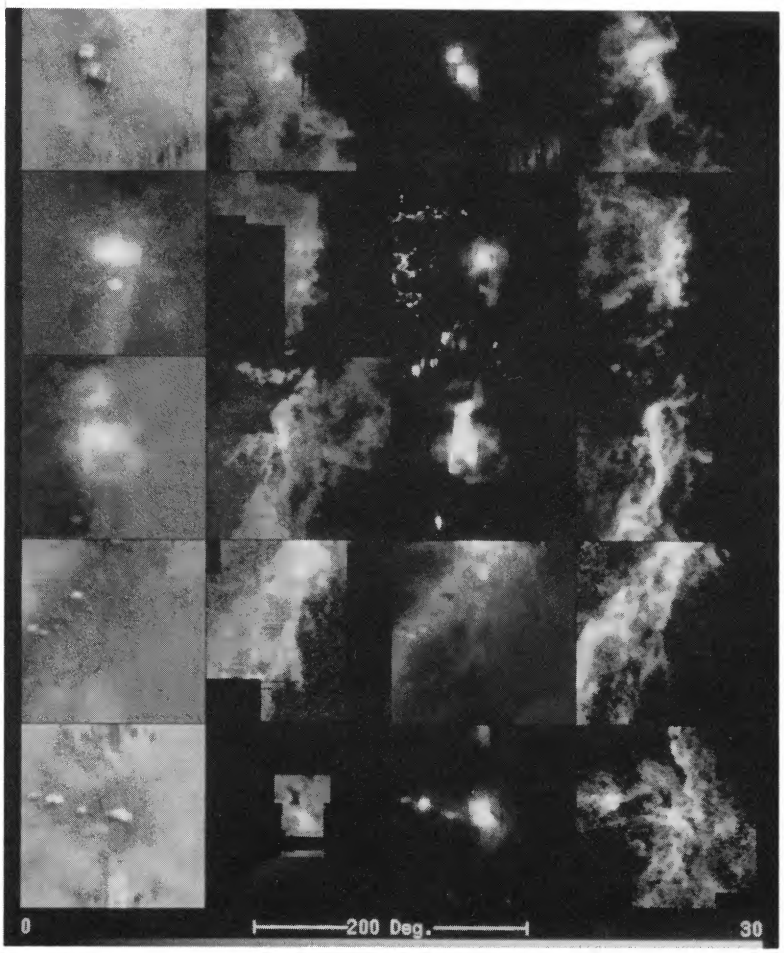

FIG. 2*b*.—Mosaic of images showing five 2°.25 × 2°.25 areas using the *IRAS* co-adds and the AT&T Bell Laboratories 7 m data for NGC 2071 and NGC 2068 (*top row*); Orion B including NGC 2024 and NGC 2023 (*second row*); Orion A including M42 and NGC 1977 (*third row*); L1641 (*fourth row*); and Mon R2 (*bottom row*). Quantities shown in each column are (*from left to right*): 60 μm/100 μm dust color temperature (20–200 K), peak ^{12}CO temperature (0–80 K), 100 μm optical depth in the large grain model (10^{-5} to 10^{-3}), and $I(^{13}\mathrm{CO})$ (0–55 K km s^{-1}).

BALLY, LANGER, & LIU (see 383, 648)

In order to put the results in Figures 1 and 2 onto a more quantitative basis, we have generated plots of the relationships between dust and gas properties using most of the pixels in the co-added images of these subfields. Figure 3 shows the relation of LGM dust opacity, $\tau(100)$, and 100 μm intensity versus integrated ^{13}CO [denoted $I(^{13}\mathrm{CO})$] emission from all subfields but separated into high- and low-luminosity regimes. Areas of high and low infrared luminosity occupy two distinct regions in these scatter plots, and the low-luminosity region can be divided further. Although $\tau(100)$ correlates better than the intensity with $I(^{13}\mathrm{CO})$, the correlation is not as good as found in B5 by Langer et al. (1989). This difference results from the wider range of radiation intensity and heating conditions encountered in Orion. To analyze these differences in more detail we discuss separately the data for each subfield.

3.1. *A Region with No Star Formation: An Outlying Portion of L1641*

The L1641 cloud is located in the southern portion of Orion, about 7° south of the center of the Orion OB I association. We have selected a portion of L1641 containing no compact infrared or stellar sources with $L > 1\ L_{\odot}$. The physical conditions are similar to those in the dark cloud Barnard 5 except that we estimate that the interstellar radiation field (hereafter denoted ISRF) at the surface of the cloud exposed to direct illumination from the Orion OB association is about 3–10 times greater than the standard value in the local interstellar medium. Note that ISRF includes all radiation relevant to grain heating ($\lambda \approx 0.1$–1 μm), distinct from that which heats the gas (primarily UV with $\lambda \approx 0.1$–0.2 μm). Our estimate of the ISRF is based on the distance of the cloud from the center of the

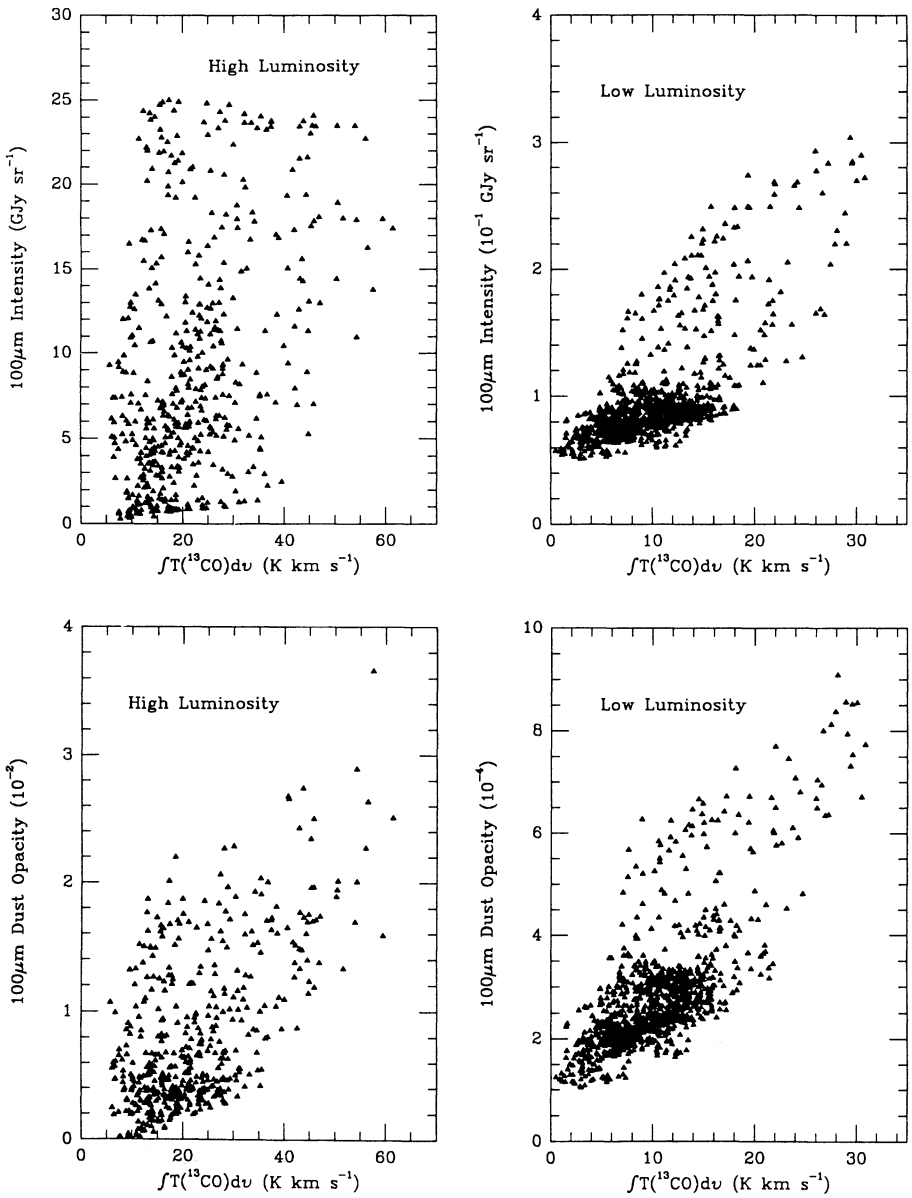

FIG. 3.—Global comparison of *IRAS* 100 μm emission and opacity vs. ^{13}CO integrated intensity separated into two parts according to luminosities

Orion OB I association whose luminosity below 1 μm is estimated by Goudis (1982) to be $L \approx 10^6\ L_\odot$.

We have selected an 18′ × 15′ portion of this cloud as an example of a region of no-star formation which is located about 10′ to the east and 30′ to the south of NGC 1999. There are no known IR point sources in this region, and the infrared emission is much weaker than that from the nearby region NGC 1999; Figure 4 shows scatter plots of various dust and gas quantities for this field in L1641. We have made a linear fit to the 100 μm intensity and $I(^{13}CO)$, $Y = kX + b$, and tabulate the coefficients k and b, along with an estimate of their uncertainties, in Table 2. The uncertainties are derived by the χ^2 method using the procedures outlined in Press et al. (1986). A measure of the average deviations of the points from the fit, σ, is also listed. The 100 μm dust opacity $\tau(100)$ correlates better than 100 μm intensity with $I(^{13}CO)$ (see Fig. 4 and Table 2). The $\tau(100)/I(^{13}CO)$ ratio is close to that found in B5 which is an isolated dark cloud with only low-mass star formation.

The correlations between IR intensity and opacity versus $I(^{12}CO)$ are not as good as the corresponding ^{13}CO correlations. However, surprisingly, a better correlation is obtained using the ^{12}CO peak temperature rather than $I(^{12}CO)$ (Fig. 4). Furthermore, it is interesting that the dust color temperature appears to be anticorrelated with the ^{12}CO peak temperature (Fig. 4). The fits between dust and gas properties in this outlying dark region of L1641 are summarized in Table 2.

3.2. *Low-Mass Star-Forming Regions in L1641*

The east side of the L1641 cloud contains a region of low-mass star formation. To analyze the dust properties, we exclude lines of sight that intercept embedded sources because the infrared fluxes are dominated by dust near the stars (see Appendix A in Langer et al. 1989). The scatter plots of the dust and gas emission in this region are shown in Figure 5, and the linear fits are given in Table 2. The correlations of 100 μm intensity and the LGM opacity with $I(^{13}CO)$ are nearly as

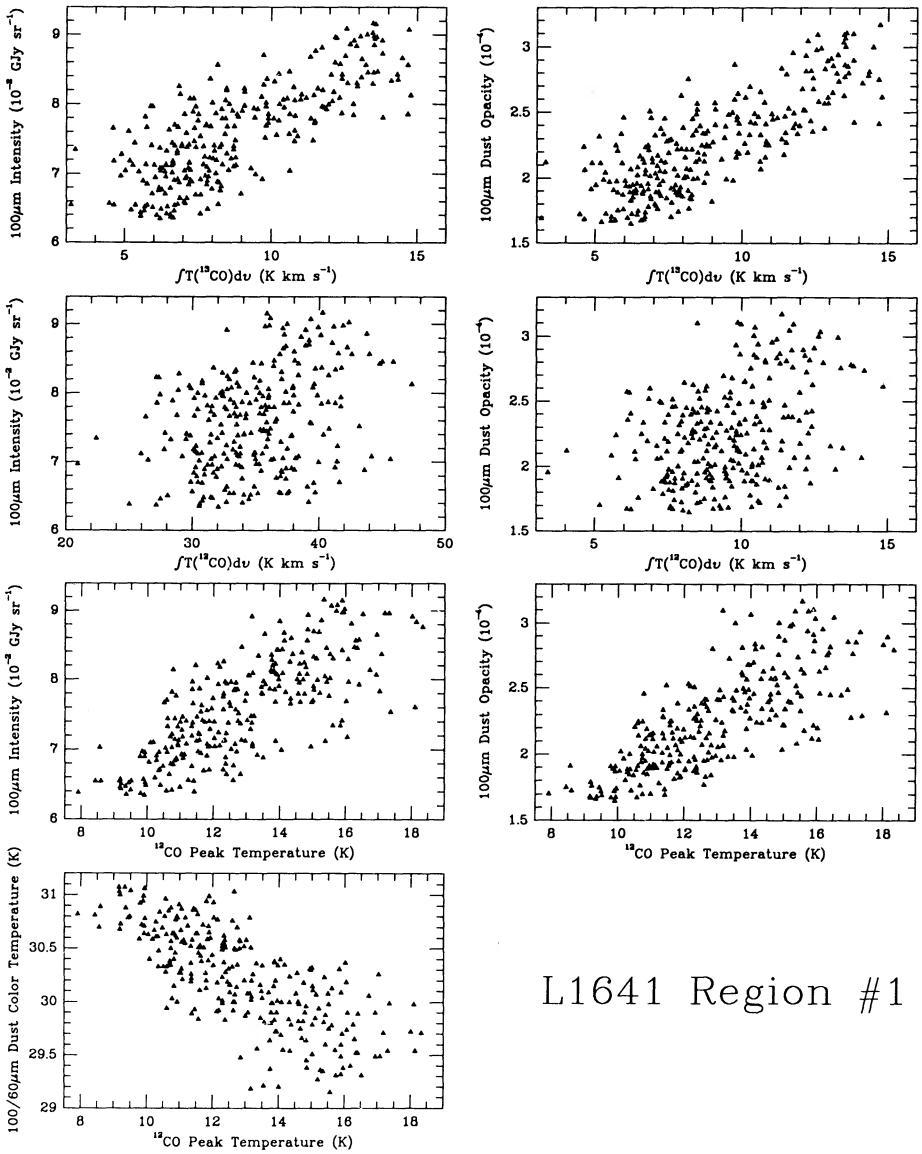

FIG. 4.—Comparison of dust and gas properties in an outlying dark region of L1641 cloud with no apparent star formation

TABLE 2

LINEAR FITS TO DUST AND GAS PROPERTIES

$Y = kX + b$

Y	X	k	b	σ
Outlying Dark Region of L1641				
I	$I(^{13}CO)$	2.3 ± 0.10	56 ± 0.95	4.5
τ	$I(^{13}CO)$	$(1.1 \pm 0.050) \times 10^{-5}$	$(1.3 \pm 0.046) \times 10^{-4}$	2.2×10^{-5}
I	$T_p(^{12}CO)$	2.7 ± 0.13	4.0 ± 1.7	4.7
τ	$T_p(^{12}CO)$	$(1.4 \pm 0.067) \times 10^{-5}$	$(3.8 \pm 0.88) \times 10^{-5}$	2.4×10^{-5}
T_{dust}	$T_p(^{12}CO)$	-0.19 ± 0.0086	32.7 ± 0.11	0.31
Low-Mass Star-Forming Region of L1641				
I	$I(^{13}CO)$	4.0 ± 0.099	50 ± 0.94	9.4
τ	$I(^{13}CO)$	$(1.7 \pm 0.044) \times 10^{-5}$	$(1.0 \pm 0.042) \times 10^{-4}$	4.2×10^{-5}
I	$T_p(^{12}CO)$	5.0 ± 0.098	25 ± 1.3	8.4
τ	$T_p(^{12}CO)$	$(1.9 \pm 0.045) \times 10^{-5}$	$(3.8 \pm 0.57) \times 10^{-6}$	3.8×10^{-5}
T_{dust}	$T_p(^{12}CO)$	-0.35 ± 0.0070	34.3 ± 0.090	0.60
Haro 4-255				
I	$I(^{13}CO)$	11 ± 0.84	-51 ± 11	19
τ	$I(^{13}CO)$	$(4.4 \pm 0.23) \times 10^{-5}$	$(-2.9 \pm 0.31) \times 10^{-4}$	5.2×10^{-5}
NGC 1999				
I	$I(^{13}CO)$	8.1 ± 0.54	-39 ± 9.5	44
τ	$I(^{13}CO)$	$(2.5 \pm 0.16) \times 10^{-5}$	$(1.0 \pm 0.28) \times 10^{-4}$	1.3×10^{-4}
I	$I(^{12}CO)$	2.8 ± 0.19	-33 ± 14	42
τ	$I(^{12}CO)$	$(8.8 \pm 0.48) \times 10^{-6}$	$(-1.3 \pm 0.37) \times 10^{-4}$	1.1×10^{-4}
I	$T_p(^{12}CO)$	16 ± 0.75	-183 ± 17	32
τ	$T_p(^{12}CO)$	$(4.5 \pm 0.27) \times 10^{-5}$	$(-4.6 \pm 1.2) \times 10^{-4}$	1.2×10^{-4}
NGC 2024				
I	$I(^{13}CO)$	$(5.0 \pm 0.3) \times 10^{2}$	$(-5.0 \pm 0.74) \times 10^{3}$	4.4×10^{3}
τ	$I(^{13}CO)$	$(4.9 \pm 0.25) \times 10^{-4}$	$(-4.9 \pm 0.63) \times 10^{-3}$	3.8×10^{3}
Monoceros R2				
I	$I(^{13}CO)$	$(3.8 \pm 0.19) \times 10^{2}$	$(-3.8 \pm 0.46) \times 10^{3}$	2.0×10^{3}
τ	$I(^{13}CO)$	$(5.0 \pm 0.36) \times 10^{-4}$	$(-5.0 \pm 0.86) \times 10^{-3}$	3.8×10^{-3}
I	$I(^{12}CO)$	94 ± 7.1	$(-1.9 \pm 0.60) \times 10^{3}$	2.7×10^{3}
τ	$I(^{12}CO)$	$(1.2 \pm 0.094) \times 10^{-4}$	$(-4.9 \pm 0.79) \times 10^{-3}$	3.5×10^{-3}
I	$T_p(^{12}CO)$	$(8.2 \pm 0.68) \times 10^{2}$	$(-8.2 \pm 1.2) \times 10^{3}$	3.0×10^{3}
τ	$T_p(^{12}CO)$	$(1.1 \pm 0.11) \times 10^{-3}$	$(-1.4 \pm 0.19) \times 10^{-2}$	4.6×10^{-3}
T_{dust}	$T_p(^{12}CO)$	-1.3 ± 0.21	63 ± 3.8	9.3
Orion Nebula (M42)				
I	$I(^{13}CO)$	$(6.7 \pm 0.44) \times 10^{2}$	$(-1.7 \pm 1.1) \times 10^{3}$	6.7×10^{3}
τ	$I(^{13}CO)$	$(5.5 \pm 0.35) \times 10^{-4}$	$(-2.3 \pm 0.85) \times 10^{-3}$	5.3×10^{-3}
I	$I(^{12}CO)$	$(1.8 \pm 0.44) \times 10^{2}$	$(-1.6 \pm 0.008) \times 10^{5}$	4.7×10^{3}
τ	$I(^{12}CO)$	$(1.4 \pm 0.035) \times 10^{-4}$	$(-1.2 \pm 0.064) \times 10^{-2}$	3.8×10^{-3}
I	$T_p(^{12}CO)$	$(7.5 \pm 0.18) \times 10^{2}$	$(-1.0 \pm 0.0068) \times 10^{5}$	3.9×10^{3}
τ	$T_p(^{12}CO)$	$(3.8 \pm 0.16) \times 10^{-4}$	$(-2.8 \pm 0.62) \times 10^{-3}$	3.5×10^{-3}

NOTES.—I and τ denote 100 μm intensity in MJy sr^{-1} and dust opacity, respectively; T_{dust} denotes 100/60 μm color temperature; and $I(^{13}CO)$ and $I(^{12}CO)$ are both in K km s^{-1}.

good as those found in regions with no known star formation. Although there is no correlation between 100 μm opacity or 100 μm intensity with $I(^{12}CO)$, there is a correlation between 100 μm intensity and opacity with ^{12}CO peak temperature. As in the portions of L1641 where no star formation is taking place, the LGM dust color temperature decreases with ^{12}CO peak temperature up to $T_{peak} = 15$ K, beyond which it levels off or perhaps turns up slightly. Comparison of the fits given in Table 2 shows that the $\tau(100)/I(^{13}CO)$ ratio inferred from the *IRAS* data (see § 4) is higher in regions of low-mass star formation than in regions with no known star formation.

3.3. *Intermediate-Mass Star-Forming Regions*

3.3.1. *Haro 4-255 and Re 50 in L1641*

We selected two isolated intermediate star-forming regions in Orion as examples. The two regions, containing Haro 4-255 (Levreault 1988) and Re 50 (Reipurth & Bally 1985), are located in the southern part of the L1641 cloud. Haro 4-255 has an infrared luminosity of 30 $L_\odot$ while Reipurth 50 has 170 $L_\odot$. Both infrared sources are associated with molecular bipolar outflows, indicating that they are extremely young stars, and Re 50 contains an extremely bright and time variable

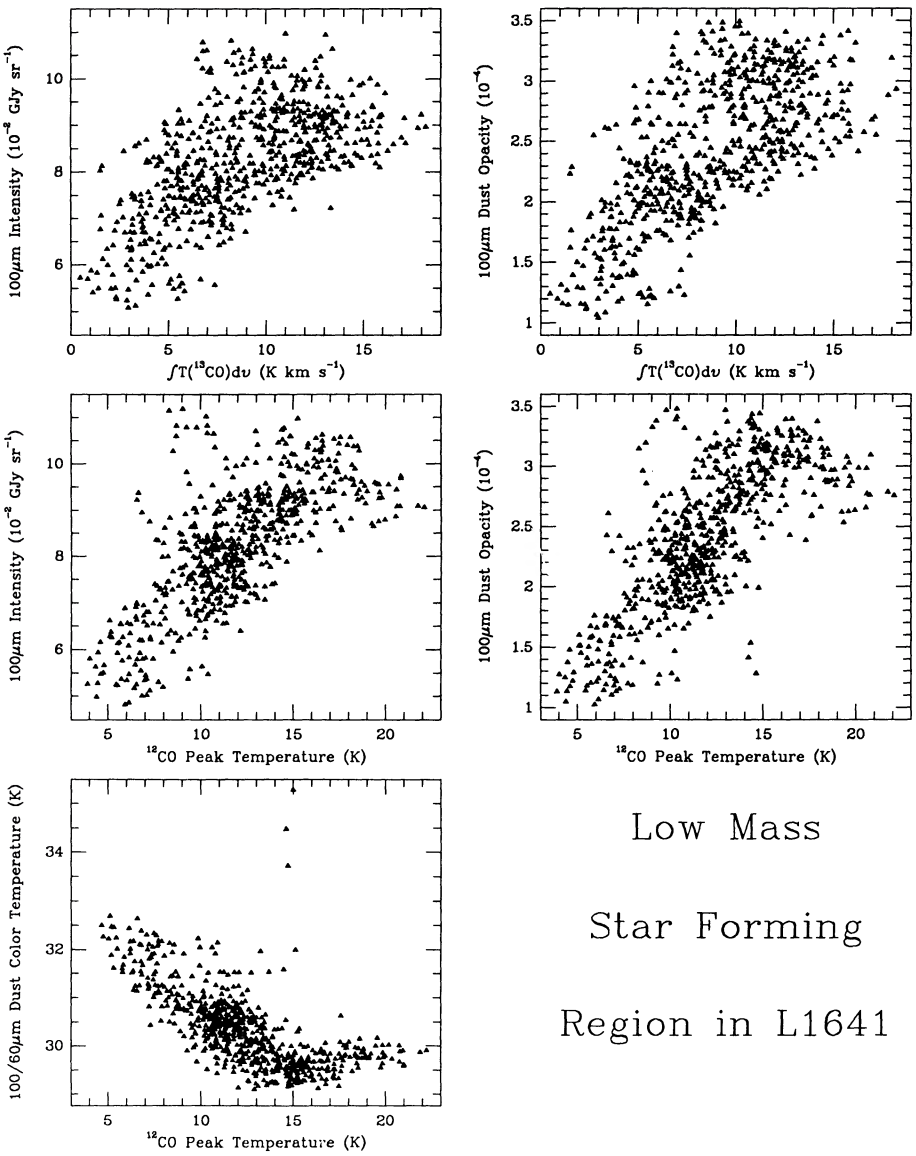

FIG. 5.—Comparison of dust and gas properties in the low-mass star-forming region of the L1641 cloud

reflection nebula (Reipurth & Bally 1985). Near Haro 4-255, the 100 μm intensity is not well correlated with $I(^{13}CO)$ although the dust opacity exhibits a reasonable relationship (Table 2). There is no correlation between LGM dust opacity and $I(^{13}CO)$ in Re 50.

3.3.2. *The NGC 1999 Region*

NGC 1999 is a reflection nebula illuminated by the star V380 Orionis in the northern portion of L1641 (Herbig 1960; Warren-Smith et al. 1980; Warren-Smith 1983). Several Herbig-Haro objects and infrared sources (including HH 1 and 2) are buried in a massive cloud core located several arcminutes to the southwest (Morgan et al. 1991). The IR and CO emission peaks in the region of NGC 1999 have similar morphology. The 100 μm intensity and LGM dust opacity correlate well with both $I(^{13}CO)$ and the ^{12}CO peak temperature (not shown here). Unlike the low-luminosity regions discussed above, the 100 μm intensity and LGM dust opacity appear to be linearly related to $I(^{12}CO)$. The gas and dust temperatures show little correlation, and there is a large spread in their values.

Most reflection nebulae are associated with intermediate luminosity sources. An interesting pattern to emerge for these nebulae is that, on average, the scatter plots exhibit a relatively larger spread in values than either the high-luminosity, or the low-luminosity, sources. A possible explanation for this effect may be that reflection nebulae contain a greater diversity of radiation field environments in the field of view. While the ^{13}CO emission is relatively insensitive to the radiation field in these sources, both the 100 μm and optically scattered light is highly sensitive to the radiation flux incident on the cloud surface. Regions like NGC 2023 or Re 50 contain both highly irradiated and lightly irradiated cloud surfaces—a greater diversity of environments than found in low-mass star-forming regions or near very luminous regions where essentially all of the projected surface area of the gas is bathed in strong radiation, and where along almost all lines of sight, the dust is somewhere hot enough to radiate at 100 μm.

3.4. *Regions Containing Stars Earlier Than B5*

The more luminous star-forming regions in Orion such as NGC 2071, NGC 2068, NGC 2024, NGC 2023, NGC 1977, and M42 contain clusters of stars which may be gravitationally bound by the mass of the molecular gas but not by the mass of the cluster itself. The clusters contain from at least 50 stars (NGC 2023) to over 500 stars in NGC 2024 (Lada 1989) and M42 (McCaughrean 1988), which collectively heat the surrounding gas and dust.

Near H II regions, the heating radiation can be many orders of magnitude greater than the ISRF due to the presence of the massive stars. The luminosity of a single ionizing star with more than 20 $M_\odot$ is comparable to the total flux of ISRF absorbed by an entire 10^5 $M_\odot$ giant molecular cloud (GMC). Due to the intensity of the radiation field, dust grains surrounding H II regions are hot. Below, we analyze several such regions with locally generated luminosities in the range 10^3–10^5 $L_\odot$.

3.4.1. *Regions Containing B0 to B3 Stars*

NGC 2071 and NGC 2068 are two reflection nebulae associated with compact H II regions about 2° to the north and 70′ to the east of NGC 2024 in the northern portion of the Orion B molecular cloud. In 100 μm emission, NGC 2071 is spherically symmetric, while in ^{13}CO and ^{12}CO emission, the cloud is elongated. The 100 μm and CO emission peaks coincide within a few arcminutes. The large scatter in the plots (Fig. 6, *top*) of $\tau(100)$ and $I(100)$ versus integrated ^{13}CO emission reflect this difference in morphology. We omit the figures and fits for NGC 2068 since they show a behavior similar to NGC 2071. NGC 2023 is a small reflection nebula located about 20′ to the south of the H II region NGC 2024. The centers of the *IRAS* and ^{13}CO emission coincide, but the correlation between the IR and ^{13}CO emission show a large scatter. This feature appears to be a general property of all reflection nebulae in Orion (Re 50, NGC 1999, NGC 2071, and NGC 2068).

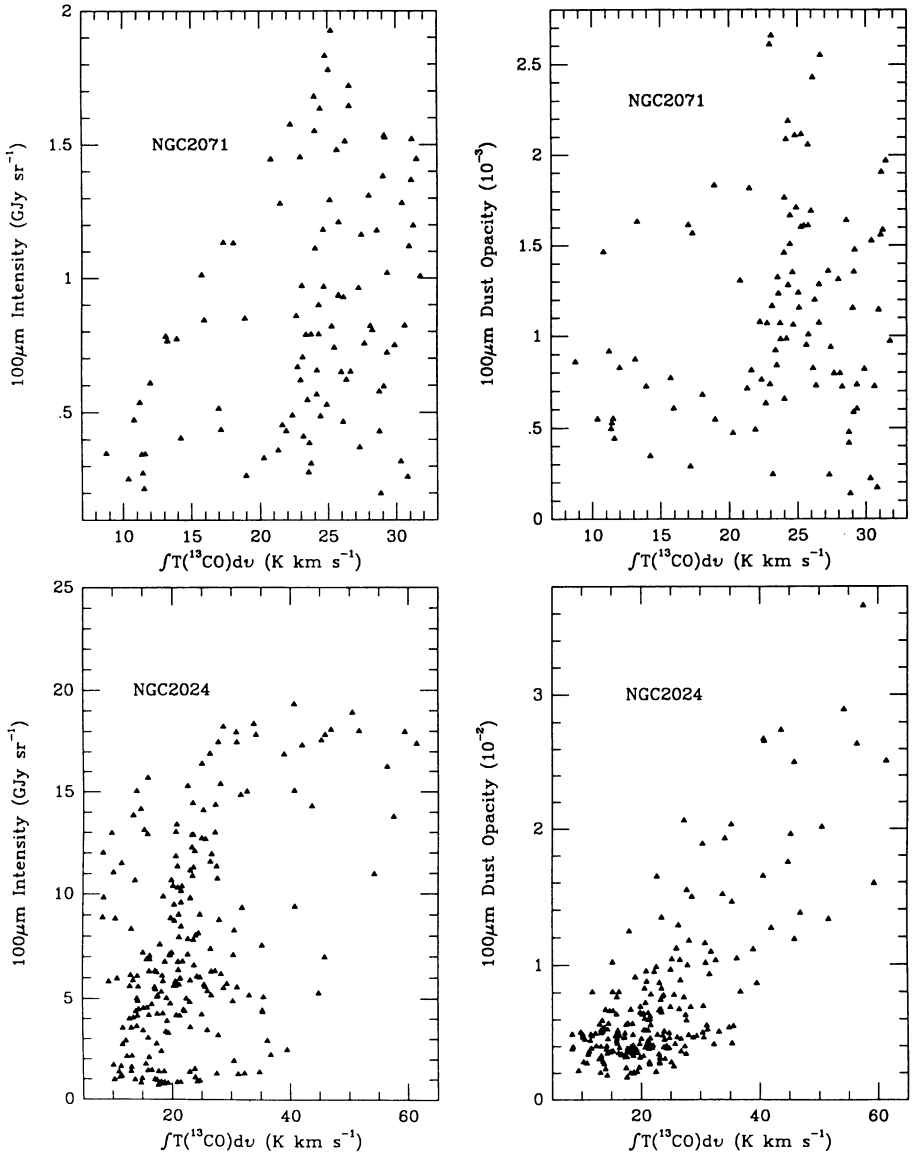

FIG. 6.—Comparison of dust and gas properties in the intermediate-luminosity region surrounding NGC 2071 (*top*) and the high-luminosity region containing NGC 2024 (*bottom*).

3.4.2. *Regions Containing O Stars: the NGC 2024 Region*

NGC 2024 is the second most luminous source in the Orion region. The 100 μm intensity map is round and centered on a dust lane which divides the nebula in the middle (Malin 1979). The peaks of 100 μm and ^{13}CO emission coincide, suggesting that this position is where the main cloud core and dominant source of luminosity are located. Although the 100 μm intensity correlates poorly with $I(^{13}\mathrm{CO})$, $\tau(100)$ correlates well (Table 2). The LGM dust temperature distribution is asymmetric in this source as shown in Figure 2. The dust grains are colder to the north and south of NGC 2024 than to the east and west. Radiation may be blocked more effectively toward the north and south by a dense wall of gas and dust outside the H II region.

3.4.3. *Monoceros R2*

Monoceros R2 is a cluster of optical reflection nebulae located behind the Orion complex at a distance of 850 pc (Racine 1968). A luminous central cluster of 5×10^4 $L_\odot$ (Thronson et al. 1980) marks an active site of massive star formation which has produced the largest known bipolar CO outflow to date (4 pc long, 200 $M_\odot$; Wolf, Lada, & Bally 1990). The peaks of CO and IR emission coincide with the infrared cluster. Despite the intense radiation field and variety of conditions encountered in this region, good correlations exist between 100 μm intensity and LGM opacity with $I(^{13}\mathrm{CO})$. A striking anticorrelation between the LGM dust color temperature and the ^{12}CO peak temperature is shown in Figure 7 and indicated in Table 2. A ring of cold dust surrounds the hot Mon R2 cloud core and is shown in a plot of the dust temperature along an east-west slice through the H II region (Fig. 7). Dust grains in the LGM have a temperature of about 80 K in the center near the compact H II region. In an annular zone extending from 5′ to 20′ from the core the dust reaches an apparent temperature minimum of about 30 K beyond which it warms up slightly to about 35–40 K. Although this behavior

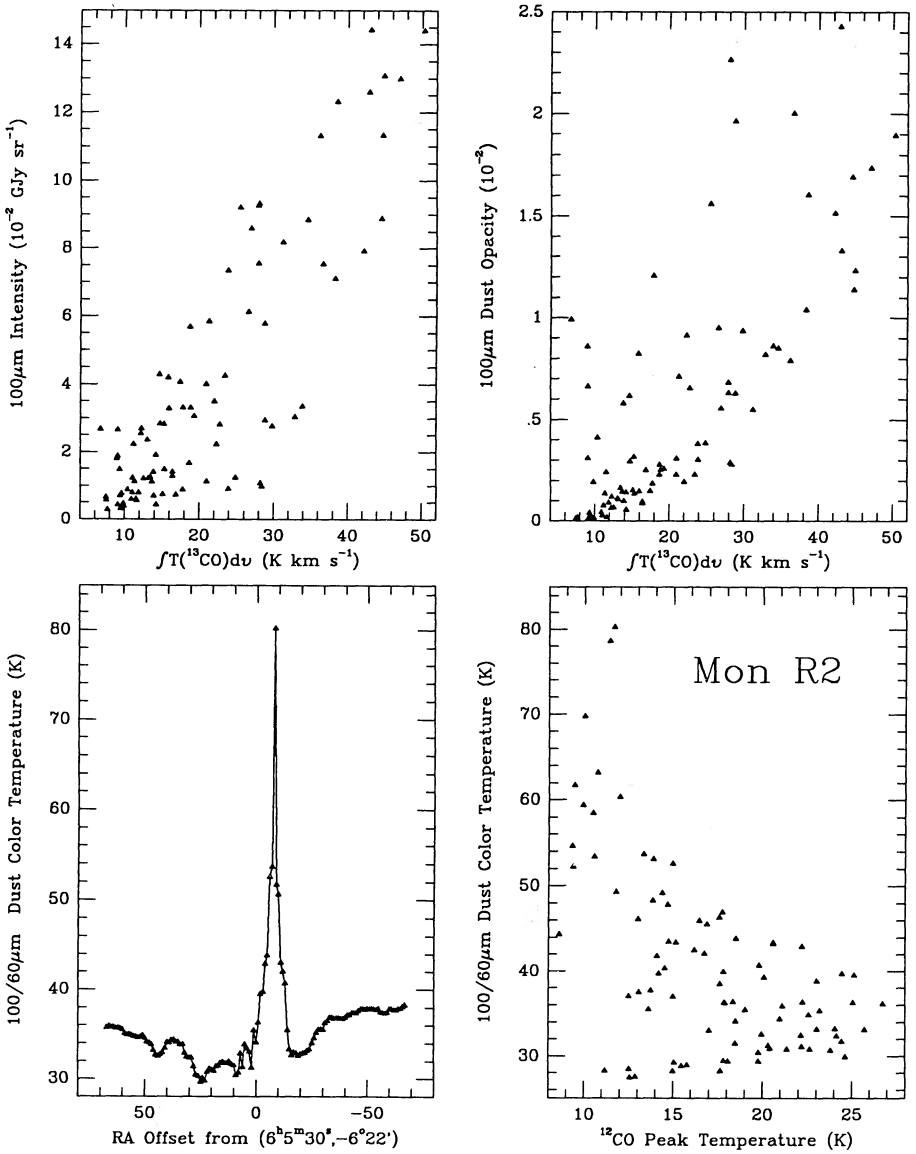

FIG. 7.—Comparison of *IRAS* 100 μm emission and ^{13}CO integrated intensity in the Monoceros R2 region. A slice cut of the dust temperature, derived using LGM, from east to west through the infrared peak of the H II region is also shown.

is seen in all regions containing luminous IR sources, it is most obvious in the Mon R2 region.

3.4.4. *Orion Nebula (M42) and NGC 1977*

The H II region M42, the most luminous region in our study, is located in the midsection of a 1° long north-south filament of high density [on average, $n(H_2) > 10^4$ cm^{-3}] gas in the northern portion of the Orion A molecular cloud (see the photographic illustration of the ^{13}CO emission in Bally et al. 1987a). The H II region forms a blister on the near side of the molecular ridge which contains a high-luminosity embedded source, IRc 2, located at a projected distance of only 1′ north of the Trapezium cluster (which is responsible for ionizing the visible nebula). The infrared morphology of M42 is very different from that of the molecular cloud; all four *IRAS* bands show M42 to consist of a very bright core surrounded by a ring of emission located just outside the optical boundary of the H II region.

A less luminous and more evolved H II region, NGC 1977, is located at the northern end of the molecular ridge. Just like M42, this region is also surrounded by a ring of infrared emission, a morphology very different from that of the associated molecular cloud.

In a 15′ × 12′ region which contains the core of the Orion A cloud and the Orion Nebula (M42), neither the 100 μm intensity nor opacity appears to correlate well with $I(^{13}CO)$ (Fig. 8). However, these quantities do correlate with $I(^{12}CO)$ up to about 200 K km s^{-1} corresponding to $I(100\ \mu m)$ of about 20 GJy sr^{-1}. At higher values of $I(^{12}CO)$, the dust opacity and 100 μm intensity do not vary. These high values correspond to the BN-KL source and the high-velocity outflow surrounding IRc 2. The north-south cuts through the BN-KL source in all four bands show that the peaks in 100 and 60 μm emission are flat, while 25 and 12 μm emission exhibit sharp peaks, suggesting saturation in the long-wavelength bands.

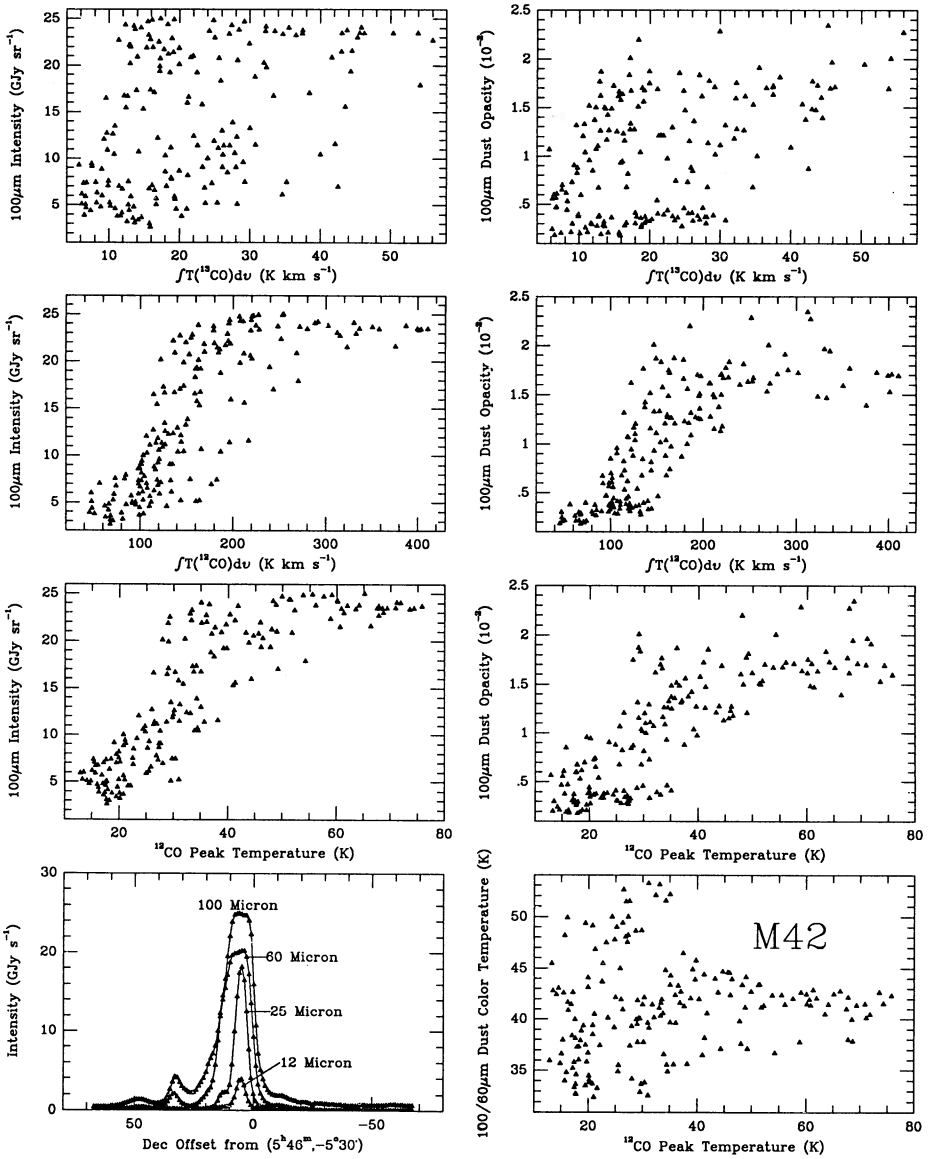

FIG. 8.—Comparison of dust and gas properties near the Orion Nebula (M42 region). Slices of intensities in all the four bands from north to south across the infrared peak of the H II region are also shown.

4. DUST PROPERTIES AND THE RADIATION FIELD

As shown in the previous section the dust properties derived using the large grain model depend on the region studied. The analysis presented in § 3 was limited to subareas of the available images. However, the results apply generally to the entire mapped region as can be seen by inspection of the images of dust and gas parameters shown in Figure 2. Columns 1 and 2 illustrate the behavior of the LGM dust temperature derived from the 60 and 100 μm flux and the ^{12}CO peak temperature which are anticorrelated in low-radiation environments. For example, in the fourth row which shows the L1641 region of Orion, the dark (cold) regions of the T_{dust} image correspond to the bright regions in both CO isotopes. The images clearly demonstrate that on average, the dust radiating at 100 μm is colder inside molecular clouds than outside.

Near luminous sources, the T_{dust} image is bright. Unlike in the CO maps, the more luminous regions, such as M42 and NGC 1977, are surrounded by rings of hot dust whose sizes are similar to the optical extent of the ionized regions. The rings may be produced by grains lying just outside ionization fronts which are propagating into mostly atomic gas. Where the cloud is illuminated from the side, such as the region near NGC 2024 and NGC 2023 (*second row*), the ^{12}CO peak gas temperature and T_{dust} is limb-brightened with a very abrupt cutoff toward the direction of the exciting stars.

Away from the bright H II regions, the large-scale structures seen in the peak ^{12}CO, $\tau(100\ \mu m)$, and $I(^{13}CO)$ are similar. The third and fourth columns of Figure 2 illustrate that LGM opacity, $\tau(100\ \mu m)$, correlates with the $I(^{13}CO)$ images. However, the dynamic range of the former is much greater than the latter. The derived dust optical depth is much greater near high-luminosity sources than in cold regions with similar $I(^{13}CO)$. The appearance of the north-south Orion A ridge situated behind the Orion Nebula dramatically illustrates this behavior. The LGM dust opacity image closely traces the warm northern portion of the molecular ridge (see Castets et al. 1990), but the southern portion of this ridge, which is just as bright in $I(^{13}CO)$, is barely visible in the dust opacity image in Figure 2. We interpret this result as a consequence of the hotter dust temperature in the north which results in more efficient 60 and 100 μm radiation from large grains.

As indicated by the correlation analysis of small subfields, in some regions, the peak ^{12}CO temperature–$\tau(100)$ correlation has less scatter than the $I(^{13}CO)$–$\tau(100)$ correlation. This difference may result from the greater amount of small-scale structure in the ^{13}CO image than in either the ^{12}CO image or the $\tau(100)$ image.

In the low-luminosity regions the slopes and offsets of the correlations between the dust parameters derived from the LGM and the gas column density as traced by $I(^{13}CO)$ are different from those in high-luminosity regions. In Table 3 we present the relationships among $I(100)$, $\tau(100)$, and $I(^{13}CO)$ as a function of several measures of the radiation field. Column 4 is the total luminosity from all associated sources of energy (cf. Goudis 1982; Mozurkewich, Schwartz, & Smith 1986). Column 5 lists the total 100 μm luminosity obtained by integrating the flux over the areas of influence surrounding each source whose boundaries are determined from the lowest approximately circular contour surrounding each region in the 100 μm *IRAS* co-adds. The 100 μm surface brightness in each region is calculated by dividing the 100 μm luminosity by its corresponding area (given in Table 3).

Below, we discuss the implications of the relationships between the dust and gas properties derived using the LGM as a function of regional luminosity and 100 μm flux. We then discuss the application of a multicomponent grain model. First we review the radiation sources in Orion to estimate the incident radiation field.

4.1. *The Radiation Field in Orion*

The radiation field impinging on the surfaces of molecular clouds in the Orion region is generally greater than the ISRF value adopted for isolated regions of the local ISM due to the large number of massive stars in the Orion OB I association (see Goudis 1982 for a review). The association contains at least 20 stars earlier than B3 and several hundred late B and A stars. The total luminous output of the OB association is estimated to be about $10^6\ L_\odot$. The flux decreases approximately as the inverse square of the distance from the center of the association for distances greater than its core radius. The radiation field energy density is $\approx 7 \times 10^2 L_6\, r_{pc}^{-2}$ (eV cm^{-3}) where L_6 is the luminosity in units of $10^6\ L_\odot$. For a characteristic distance of 40 pc (which corresponds to a 5° angle at a distance of 500 pc), the energy density is about 0.4 eV cm^{-3} for $10^6\ L_\odot$. Roughly 10% of this radiation is in the form of UV photons which can heat the gas in photodissociation regions (PDRs). This energy density is much larger than the UV radiation field near the Sun, $G_0 \approx 3.3 \times 10^{-2}$ eV cm^{-3} (the Habing field; see Tielens & Hollenbach 1985). In the Orion clouds, the UV radiation field intensity varies from G_0 to much greater values.

TABLE 3

GLOBAL RELATIONSHIPS BETWEEN DUST AND GAS

Region (1)	$I(100)/I^{13}$ ([MJy sr^{-1}]/[K km s^{-1}]) (2)	$\tau(100)/I^{13}$ (1/[K km s^{-1}]) (3)	Luminosity ($L_\odot$) (4)	Surface Brightness (MJy sr^{-1}) (5)	Area (sr) (6)	Flux (Jy) (7)
L1641 No. 1	2.3	1.1×10^{-5}	...	33	2.5×10^{-5}	8.2×10^2
L1641 No. 2	4.0	1.7×10^{-5}	...	47	6.8×10^{-5}	3.2×10^3
Haro 4-255	11	4.4×10^{-5}	3.0×10^1	57	5.9×10^{-6}	2.5×10^3
NGC 1999	8.1	2.5×10^{-5}	1.5×10^2	1.4×10^2	1.8×10^{-5}	2.5×10^3
NGC 2071	...	5.6×10^{-5}	7.0×10^2	2.8×10^2	3.5×10^{-5}	9.9×10^3
NGC 2068	...	1.25×10^{-4}	1.0×10^3	4.5×10^2	4.2×10^{-5}	1.9×10^4
NGC 2023	...	7.5×10^{-5}	2.3×10^3	6.3×10^2	1.5×10^{-5}	9.4×10^3
NGC 2024	5.0×10^2	4.9×10^{-4}	4.7×10^4	2.1×10^3	1.0×10^{-4}	2.1×10^5
Mon R2	3.8×10^2	5.0×10^{-4}	5.0×10^4	3.9×10^2	1.0×10^{-4}	3.9×10^4
M42	6.7×10^2	5.5×10^{-4}	1.0×10^5	2.7×10^3	1.8×10^{-4}	4.8×10^5

NOTES.—L1641 No. 1 refers to the outlying region with no known star formation in L1641; L1641 No. 2 refers to the low-mass star-forming region in L1641.

Local heating by embedded sources dominates the radiation field intensity in obscured star-forming cloud interiors. The radiation field near embedded sources can be estimated from counts of *IRAS* point sources or near-infrared objects and their luminosities. The co-adds contain about 1500 individual point sources in the region covered by our ^{13}CO survey. Lada (1989) has shown that in a 4 deg^2 portion of the Orion B cloud there are about 900 2 μm sources. Between 50% and 95% are members of dense transient star clusters associated with the cloud cores near NGC 2024, NGC 2023, NGC 2068, and NGC 2071. Except near the most luminous objects, such as the infrared sources in the OMC-1 core, the region influenced by embedded sources is small, characterized by the radius at which the temperature produced by radiative equilibrium is less than 10 K, $R(T < 10\ \mathrm{K}) \approx 0.4 T_{10}^{-5/2} L_2^{0.5}$ pc where T_{10} is in units of 10 K and L_2 is in units of 100 $L_\odot$. Most of the volume of the molecular clouds in Orion is heated by the external radiation field or cosmic rays rather than embedded heating sources (see Castets et al. 1990).

4.2. *The Dust-To-Gas Ratio*

The integrated ^{13}CO emission is an approximate measure of the total column density of gas in a molecular cloud. Many groups have studied the relationship between ^{13}CO and H_2 column density. For example, Langer et al. (1989) found that for the dark cloud B5, a ^{13}CO integrated intensity of 1 K km s^{-1} corresponds to a column density $N(H_2) \approx 4 \times 10^{20}$ cm^{-2}, or about 0.4 mag of visual extinction. This number assumes a ^{13}CO fractional abundance of 1.4×10^{-6} for an excitation temperature of 10 K (typical of clouds like B5). The appropriate value for Orion may be different due to different excitation conditions. The column density of gas corresponding to $I(^{13}\mathrm{CO}) = 1$ K km s^{-1} increases roughly linearly with the excitation temperature, so for $T_{ex} = 30$ K, 1 K km s^{-1} of ^{13}CO emission corresponds to about 1 mag of visual extinction, or roughly a column density of 10^{21} cm^{-2} of molecular hydrogen.

We can derive the dust-to-gas ratio in the large grain model by inserting the above relationship, which converts ^{13}CO intensity to A_V or $N(H_2)$, into the linear relationship between the 100 μm dust opacity and the ^{13}CO integrated intensity. The result is a linear relationship between $\tau(100)$ and the molecular hydrogen column density. This relationship depends on the radiation field present in each environment. In Figure 9 we plot the mean value of $\tau(100)/I(^{13}\mathrm{CO})$ as a function of the total luminosity, and the average 100 μm surface brightness for each region whose area is indicated in Table 3.

Draine & Lee (1984) have constructed a model of infrared emission based on steady state heating and a distribution of grain size assuming the Mathis-Rumpl-Nordsiek graphite-silicate grain mixture and solar metallicities and depletions. They derive a relationship $\tau(100) = 3.5 \times 10^{-25}[2N(H_2) + N(H)]$. We find that the dust opacity derived from the LGM is smaller than the predictions of Draine and Lee by a factor of 10–20 in regions of low luminosity (see Fig. 9). However, in very luminous regions the ratio of predicted to observed dust abundance is about 0.5, which implies that most of the mass of dust along these lines of sight are probed by the 60 and 100 μm flux. The differences between the dust emission characteristics of high- and low-luminosity regions can be understood in the context of varying radiation field intensities and the contribution that different subpopulations of grains make to the 60 and 100 μm flux.

Small grains make a disproportionately large contribution to the emission at 60 μm (and even 100 μm) in the presence of UV radiation. Their decreased radiative efficiency and stochastic heating produced by the absorption of individual UV photons by the smallest grains (Sellgren 1984; Puget et al. 1985; Draine & Anderson 1985) result in (time-averaged) grain temperatures which depend inversely on grain size. For the same radiation field, the small grains are warmer than the large grains.

Boulanger et al. (1988) have modeled the 60–100 μm flux

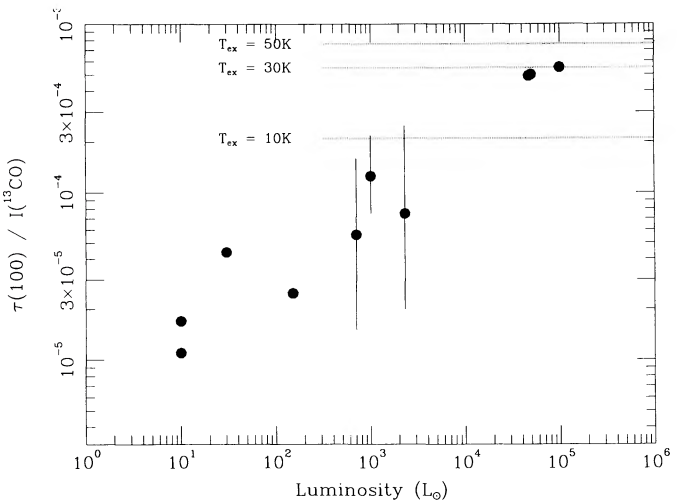

FIG. 9*a*

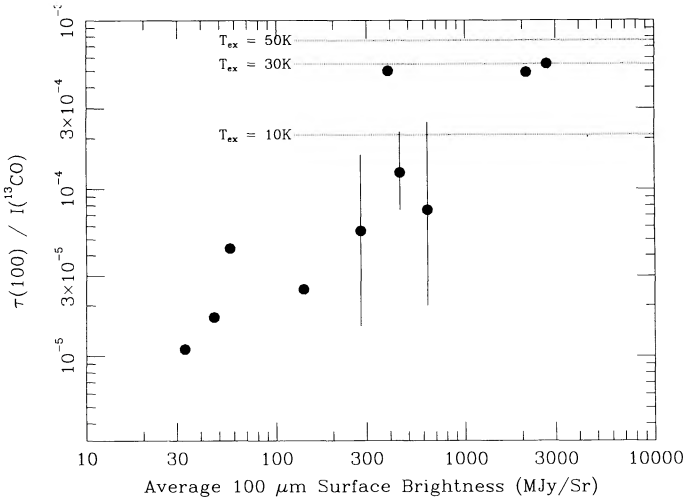

FIG. 9*b*

FIG. 9.—(*a*) Slopes of $\tau(100\ \mu\mathrm{m})$ to $I(^{13}\mathrm{CO})$ relationships given in Table 3 plotted against the total stellar luminosity in each region. For three sources, NGC 2071, NGC 2068, and NGC 2023, the average values of $\tau(100\ \mu\mathrm{m})$ to $I(^{13}\mathrm{CO})$ are plotted (*points with large error bars*). Scatter diagram analysis did not produce good correlations for these regions, and error bars indicate the range of values within which 90% of the pixels lie. The formal uncertainty for the other points is much smaller, less than twice the diameter of the plotted symbols. Horizontal dotted lines near the top illustrate the expected values of $\tau(100\ \mu\mathrm{m})$ to $I(^{13}\mathrm{CO})$ assuming the Draine & Lee dust-to-gas ratio for different choices of the ^{13}CO excitation temperature, assuming a ^{13}CO fractional abundance 1.42×10^{-6}. (*b*) Same as (*a*) except the ordinate is the average surface brightness in the areas listed in Table 3.

ratio produced by a mixture of small and large grains. The largest grains reach temperatures near that expected of a blackbody immersed in the local radiation field, while the small grains are considerably hotter, contributing most of their radiation to shorter wavelengths. Figure 4 in Boulanger et al. (1988) plots the IR intensity ratio as a function of the equilibrium temperature of large grains and compares the results for a mixture of small and large grains to the solution for large grains alone. Their work demonstrates that for large grain equilibrium temperatures of 10–20 K, most of the 60 μm and much 100 μm emission comes from small grains which determine the observed flux ratio. Above a large grain temperature of 30 K, the large grains dominate in this spectral range. It can be seen in their Figure 4 that the 60–100 μm intensity ratio decreases from 0.7 at 10 K to about 0.2 at 20 K, and increases again to about 0.7 at 40 K. Therefore a determination of fluxes and flux ratios from 60 and 100 μm alone does not give a unique solution of the large grain temperature and column density. Any given 60–100 μm intensity ratio can be produced by two possible grain temperatures, yielding two different column density solutions.

When both large and small grains are present in low-luminosity regions, use of the LGM overestimates the temperature and underestimates the total column density of the large grains. For low incident radiation fields and low resulting large grain temperatures, the 60 μm and much of the 100 μm flux is produced by the subpopulation of small grains and not by the grains which comprise most of the dust mass present in the cloud. Therefore, most of the dust remains invisible at these wavelengths.

In very luminous regions, the dust-to-gas ratio we derive is close to that predicted by Draine & Lee (1984). In the M42 and NGC 2024 cores, we find that this ratio is about a factor of 2 larger. This value of the dust-to-gas ratio implies that most of the mass of dust along these lines of sight is traced by the 100 μm flux, in reasonable agreement with the model of Boulanger et al. (1988) who predict that the 100 μm emissions in high-intensity radiation fields is dominated by large grains.

Figures 9*a* and 9*b* can be used to estimate the total dust content of a molecular cloud where the total 100 μm surface brightness or the luminosity of nearby or embedded sources is known. These plots show that the ratio $\tau(100\ \mu\text{m})/I(^{13}\text{CO})$ determined from the large grain model increases monotonically with increasing luminosity or 100 μm surface brightness. For a given determination of $I(^{13}\text{CO})$ and the luminosity or 100 μm surface brightness, averaged over a given region, Figure 9 can be used to estimate the apparent dust deficit, defined as the ratio of $\tau(100\ \mu\text{m})/I(^{13}\text{CO})$ for the region divided by the value of this ratio in luminous regions. We assume that the excitation temperature of the gas is 30 K in the luminous regions to estimate the gas column density from $I(^{13}\text{CO})$. Therefore, the dust deficit is the measured ratio $\tau(100\ \mu\text{m})/I(^{13}\text{CO})$ for the region divided by 5.5×10^{-4}. The true 100 μm dust optical depth, averaged over a region, can be estimated by multiplying $\tau(100\ \mu\text{m})$ computed using the LGM by the inverse of the dust deficit estimated from Figure 9. Figure 9*b* can be fitted by a power law with a slope of 1 so that

$$\frac{\tau(100)}{I(^{13}\text{CO})} = 3.3 \times 10^{-7} F_{100}\ (\text{MJy/sr})$$

below $F_{100} = 3000$ MJy sr^{-1} with $\tau(100)/I(^{13}\text{CO}) = 5.5 \times 10^{-4}$ for larger values of F_{100}. The true dust opacity in regions with ^{13}CO emission is approximately given by

$$\tau_{\text{true}}(100) = \frac{1.7 \times 10^3 \tau(100)}{F_{100}\ (\text{MJy/sr})}\ .$$

This relationship may be in error by about a factor of 3, based on the scatter shown in Figures 9 and 10.

Recent *COBE* observations suggest that the *IRAS* 60 and 100 μm fluxes are systematically overestimated for extended sources of emission (C. A. Beichman 1990, private communication). This error will not have a large effect on the derived LGM dust temperature (which depends on the log of the ratio of the 60–100 μm flux, and thus the error largely cancels in the dust temperature determination); however the opacities and column densities will be reduced by a factor of about 2. This reduction would bring our results for M42 and NGC 2024 into excellent agreement with the Draine and Lee model. The gas column density estimates may also be in error for two reasons: (1) As shown by Castets et al. (1990), the ^{13}CO lines may not be optically thin toward some lines of sight in the

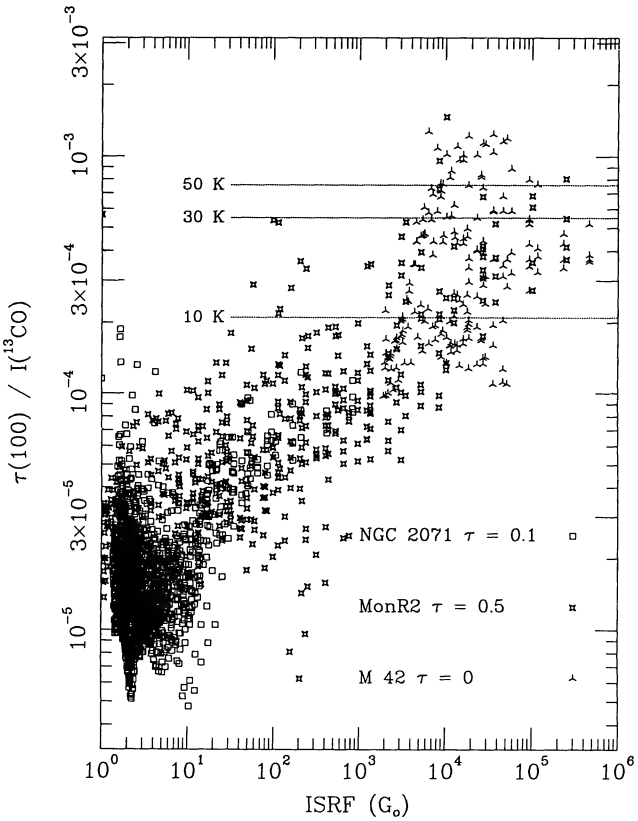

FIG. 10.—Relationship between $\tau(100\ \mu\text{m})/I(^{13}\text{CO})$ ratio in each pixel of the maps and the estimated ISRF for the regions surrounding NGC 2071, Orion A, and Mon R2. The regions considered are about 1–4 pc in radius. Region boundaries were cropped to avoid confusing sources such as NGC 2068 due south of NGC 2071. Only the portions of the images where ^{13}CO emission is brighter than about 1 K are considered in order to omit values of the dust-to-gas ratio which are dominated by noise. A common global relation requires that a source-dependent exponential decrease of radiation field intensity as a function of projected distance from the nearest major source of luminosity be included. The horizontal dotted lines near the top illustrate the expected values of $\tau(100\ \mu\text{m})$ to $I(^{13}\text{CO})$ assuming the Draine and Lee dust-to-gas ratio for different choices of the ^{13}CO excitation temperature, assuming a ^{13}CO fractional abundance 1.42×10^{-6}. Horizontal axis is in units of $G_0 \approx 3.3 \times 10^{-2}$ eV cm^{-3}, the Habing radiation field energy density. The vertical axis is in units of 1/(K km s^{-1}).

Orion clouds. In this case, the gas column densities are underestimated. (2) Kinetic temperature structure in the cloud may result in errors in the partition function corrections in calculating total column densities.

4.3. *The Dust-To-Gas Ratio Versus Local Radiation Field*

We have shown above that the dust-to-gas ratio derived using the LGM is a function of the local radiation field. We next analyze the dust-to-gas ratio on a pixel-by-pixel basis, taking account of the flux of incident radiation including the effects of geometric dilution and attenuation. To estimate the ISRF as a function of position in the cloud we need to know the luminosity of the nearby stars and the source geometry. We use the projected angular distance between any pixel in the map and the centroid of infrared emission associated with the nearest source of luminosity to estimate the flux of incident radiation.

We assume that the radiation field is given by the source luminosity and the projected distance r by

$$F = e^{-\tau} L/(4\pi r^2) ,$$

where τ is the 0.5 μm (visual) optical depth. Since our maps are on a 1′ grid, we rewrite this equation in units which makes computations easy. Expressing r in units of arcminutes scaled to the distance of Orion, the flux is given by

$$F(x, y) = 923 r^2 \left(\frac{L}{10^3\ L_\odot}\right)\left(\frac{D}{400\ \mathrm{pc}}\right)^{-2} \exp\left[-0.25 r'\left(\frac{\bar{n}}{10^3}\right)\right],$$

where $\bar{n}$ is the average density of the gas and D is the distance to the region. We assume that the dust is heated primarily by photons with a mean wavelength around 0.5 μm and that the visual optical depth is given by Figure 7 in Draine & Lee (1984) as $\tau \approx 5.5 \times 10^{-22}[N(\mathrm{H\ I}) + 2N(\mathrm{H}_2)]$. The projected distance r is derived from x_0 and y_0 which correspond to the position of the source of luminosity using $r = [(x - x_0)^2 + (y - y_0)^2]^{1/2}$.

Our estimate of the visual optical depth τ is based on the mean cloud density toward each source of luminosity estimated from the properties of the surrounding molecular cloud. We compute the average gas density in each cloud from the area-averaged column density of gas derived from $I(^{13}\mathrm{CO})$ assuming a spherically symmetric cloud model. In Figure 10, we plot the ratio $\tau(100)/I(^{13}\mathrm{CO})$ as a function of estimated ISRF flux for three regions: NGC 2071, Orion A, and Mon R2.

The Trapezium cluster, which is the dominant source of luminosity in the Orion A region, lies in the foreground between us and the surface of the molecular cloud. Optical studies indicate that there is not much dust inside the H II region. However, the H II region morphology and the large electron density in the core of M42 indicates that the distance between the stars and the cloud is only a few tenths of a parsec. Therefore, for Orion A we model the ISRF flux by an inverse-square dependence on the projected distance from the Orion A infrared luminosity centroid, and we set the visual optical depth $\tau = 0$.

The Mon R2 region contains an embedded cluster of stars visible in infrared images. The large extinction toward these sources, the lack of a prominent optical H II region, and the presence of a well-developed 30′ long bipolar CO outflow indicate that this source is still deeply embedded in a molecular cloud. In Figure 9*b*, we use $\bar{n} \approx 2 \times 10^3$ cm^{-3} which gives a visual optical depth of $\tau = 0.5$ at a projected distance of 0.21 pc.

NGC 2071 is an intermediate luminosity region with associated reflection nebulosity. To evaluate the extinction in this region, we use an $\bar{n} = 400$ cm^{-3} which corresponds to a visual optical depth $\tau = 0.1$ for a projected distance of 0.15 pc. This value is consistent with that used for Mon R2, which has a more prominent cloud core in both CO and CS lines.

As can be seen in Figure 10, this model yields a single linear relationship between the derived dust-to-gas ratio and the estimated value of ISRF flux at each point in the maps for all three sources. Ignoring visual attenuation generates a diagram in which the derived dust-to-gas ratio for various regions differs by nearly two orders of magnitude for the same estimated ISRF.

Figure 10 can also be used to estimate the dust deficit defined in § 4.2 on a pixel-by-pixel basis in a map. The monotonic relationship in Figure 10 has the same shape as the relationship between $\tau(100\ \mu\mathrm{m})/I(^{13}\mathrm{CO})$ and the 100 μm surface brightness shown in Figure 9*b* and is expressed by a power-law relationship

$$\frac{\tau(100)}{I(^{13}\mathrm{CO})} = 1.4 \times 10^{-5} G_{\mathrm{ISRF}}^{0.34} .$$

An estimate of G and a measure of $I(^{13}\mathrm{CO})$ can be used to infer the dust deficit. Multiplication of $\tau(100\ \mu\mathrm{m})$ by the inverse of this number produces an estimate of the true 100 μm dust optical depth.

Our estimate of the ISRF in each pixel of a map is related to the 100 μm surface brightness of the pixel. Comparison of the slopes of Figures 9*b* and 10 show that our estimate of G depends on F_{100} as $G \approx 1.4 \times 10^{-4} F_{100}(\mathrm{MJy\ sr^{-1}})^{2.6}$.

4.4. *Multicomponent Grain Models*

In the analysis above, we found that the dust-to-gas ratio calculated in the LGM is too small by one or two orders of magnitude over most of Orion. In colder portions of the Orion molecular clouds, a multicomponent grain model, such as that of Boulanger et al. (1988), is needed. We assume that in cold regions large grain dust temperature is given by the lower branch of the 60–100 μm flux ratio in Figure 11. In the Appendix we present an algorithm for using the 12–60 μm flux ratio as a constraint on the large grain dust temperature.

We applied this two component model by first subtracting a baseline from each image and using a threshold $I(12\ \mu\mathrm{m})/I(60\ \mu\mathrm{m})$ of 0.41. Generally, this approach produced unphysical results in the 100 μm optical depth images with abrupt jumps in the value of $\tau(100)$ in most places where the computation was forced to switch from one branch to the other. Therefore, we iteratively adjusted the image zero-points and the threshold until a spatially smooth temperature and optical depth map are produced. We found that this was only possible over small portions of the images, suggesting that two-dimensional spline fits to the image baselines are needed.

Our optical depth computation assumes that all of the 100 μm flux is produced by large grains. In principle, the small grain contribution to the 100 μm flux should be subtracted from the 100 μm flux image prior to computation of the opacity map. In practice, this subtraction can be accomplished by the removal of a fixed multiple of the 12 μm image from the 100 μm image. We did not perform this step, since the corrections to the 100 μm flux maps are small, and the extra step introduces more systematic errors.

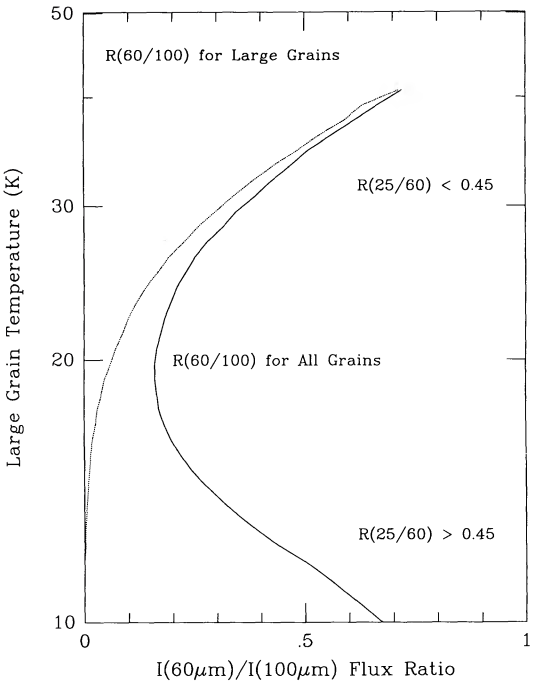

FIG. 11.—Large grain dust temperature as a function of the 60 and 100 μm flux ratio for both the large grain and the multigrain model (adapted from Fig. 4 of Boulanger et al. 1988). Use of the solid curve to estimate the large grain dust temperature is discussed in the Appendix.

Our best efforts did not produce a reasonable estimate of the large grain optical depth in cold regions of the Orion clouds. A striking failure of this application of the MCGM occurs in cold regions where the small grains are expected to dominate (lower branch of Fig. 11); the estimated 100 μm optical depth anticorrelates with the distribution of $I(^{13}\mathrm{CO})$. The $\tau(100\ \mu\mathrm{m})$ increases toward the cloud edges where the ^{13}CO emission is decreasing, a clearly nonphysical result. We suspect that the $I(60)/I(100)$ flux ratio variations do not correspond to true variations in the large grain temperature. Other factors, such as spatial variations in grain properties or variations in the fraction of the flux contributed by small grains, may be responsible.

Quantitatively, toward the ^{13}CO cores, the ratio of $\tau(100)/I(^{13}\mathrm{CO})$ exceeds the expected value by about an order of magnitude. We suspect that a straightforward application of the Boulanger et al. model to the Orion clouds underestimates the large grain temperature, resulting in an overestimation of $\tau(100)$. In this low-temperature regime, $\tau(100)$ is very sensitive to small changes in the temperature. Since $\tau(100)$ is proportional to $e^{144/T_{\mathrm{dust}}}$ for small T, a small change or uncertainty in the dust temperature, ΔT_{dust}, leads to an error $\Delta\tau/\tau \approx 144/T_{\mathrm{dust}}^2 \times \Delta T_{\mathrm{dust}}$. For a typical cold region (less than 20 K), a 10% uncertainty in dust temperature leads to a factor of 2 or more uncertainty in the $\tau(100)$. However, in warm regions ($T_{\mathrm{lg}} > 28$ K), the results are insensitive to errors and are identical to those derived using the large grain model.

4.5. *Constant Temperature Cold Large Grain Model*

Motivated by the structural correlation between the 100 μm images and the integrated ^{13}CO emission and the need to avoid the sensitivity to dust temperature uncertainties, we used the above algorithm to construct optical depth maps based on the assumption that whenever the ratio $I(12)/I(60)$ is greater than the chosen threshold (0.41), the large grain temperature is actually about 18 K, independent of the ratio $I(60)/I(100)$. Where the shorter wavelength ratio is below the threshold, the computation proceeds using the upper branch of the curve in Figure 11. This method provides a physically reasonable picture in which the $\tau(100)$ images correlate with the $I(^{13}\mathrm{CO})$ images, and the $\tau(100)/I(^{13}\mathrm{CO})$ ratio, averaged over the cold regions, gives a value close to that in the hot regions of Orion. The images of $\tau(100)$ suffer from abrupt jumps where the model switches from warm large grains, where the opacity is low, to the cold grain domain, where the dust-to-gas ratio is found to be close to Draine & Lee value. A smooth transition needs to be implemented by correctly modeling the behavior of different grain subpopulations.

Physically this model implies that in the cold regions, the long-wavelength color ratio is primarily sensitive to variations in the characteristics of the small grains, and does not reflect true variations in the large grain temperature. Furthermore, when large grains become much colder than 20 K, their low emissivities make their temperatures insensitive to the ISRF since the grains radiate every inefficiently. The empirical result, that in cold regions the 100 μm intensity maps themselves correlate with the $I(^{13}\mathrm{CO})$ maps, suggests that the large grains which radiate in the 100 μm band must be nearly at the same physical temperature, despite the variations in the $I(60)/I(100)$ ratio. We conclude that the large grains in "cold" portions of the Orion clouds have a temperature of about 18 K.

5. SUMMARY AND CONCLUSIONS

We have compared the dust emission in the Orion region observed with the *IRAS* satellite with large-scale maps of the gas distribution traced by CO. We have investigated the dust temperature and 100 μm optical depth derived from a large grain model as a function of the interstellar radiation field. We divided the data into subsets with luminosities ranging over five orders of magnitude.

5.1. *The Dust-To-Gas Ratio*

We use the *IRAS* 60 and 100 μm images to calculate the dust temperature using a large grain model (LGM). By combining this temperature with the 100 μm flux, we compute the large grain 100 μm optical depth, $\tau(100)$. We then divide $\tau(100)$ by the ^{13}CO integrated intensity, $I(^{13}\mathrm{CO})$, to produce an estimate of the dust-to-gas ratio. This method assumes that $I(^{13}\mathrm{CO})$ is optically thin and that it has roughly a constant excitation temperature and that this quantity is an estimator of the total column density of molecular gas along the line of sight. We find that our derived dust-to-gas ratio varies by two orders of magnitude in the Orion region. This measure of the dust-to-gas ratio, $\tau(100)/I(^{13}\mathrm{CO})$, ranges from 10^{-5} K^{-1} km^{-1} s (corresponding to a true dust-to-gas ratio of about 0.01% by mass) in regions far from external radiation sources and devoid of embedded objects to over 10^{-3} K^{-1} km^{-1} s (a true dust-to-gas ratio of about 1% by mass) in the cores containing luminous embedded sources or in gas and dust adjacent to H II regions. The variation of the estimated dust-to-gas ratio depends monotonically on the total luminosity of the region being considered or equivalently, the average flux of incident radiation. Figures 9 and 10 provide an empirically deduced relation between the estimated dust-to-gas ratio and the local radiation field. These plots demonstrate that a direct application of the large grain model underestimates the total dust

column density toward molecular clouds and the total dust content of these clouds cannot be reliably deduced from the 100 and 60 μm *IRAS* data, except in regions where the radiation field is more than a thousand times the typical interstellar value. Figures 9 and 10, and the power-law relations derived from them, can be used to improve the estimate of the true dust optical depth in a molecular cloud by an empirically derived correction factor.

Our interpretation of this result is that along typical lines of sight through molecular clouds, the 60 μm emission is dominated by a subpopulation of small grains, whose average temperature is higher than the temperature of the large grains containing the bulk of the dust mass. Therefore, the 60 and 100 μm color temperature is overestimated, and for a given 100 μm intensity, the large grain optical depth is underestimated, producing a low dust-to-gas ratio. Along most lines of sight through molecular clouds, the average large grain is too cold to contribute a significant amount of flux to the 60 μm and in some case even the 100 μm bands. Longer wavelength submillimeter observations, which are sensitive to dust colder than 20 K, are needed to probe the dust content throughout most of the projected area of typical molecular clouds.

As the radiation field produced by either external or embedded sources increases, the large grain temperature rises, and an increasing fraction of this dust radiates in the 60 and 100 μm *IRAS* bands. Therefore, the dust-to-gas ratio derived using the large grain model grows with increasing temperature. For sufficiently high dust temperatures, large grains contribute most to the 60 and 100 μm flux, and the derived dust optical depth and the dust temperature reflects the total of the mass in dust grains. Comparison with the ^{13}CO integrated intensity indicates that toward lines of sight along which most of the gas and dust is hotter than 40 K, the dust-to-gas ratio is within a factor of 2 of the canonical value derived from the optical extinction data.

Small-scale structure in the molecular cloud permits the penetration of the UV and optical radiation fields which heat the gas and dust as shown by the submillimeter observations of C^+ (Howe et al. 1991). The Orion clouds also contain hundreds of young embedded stars which are on or near the main sequence. Many are not heavily shrouded by circumstellar dust, and the starlight illuminates interior surfaces of the cloud. These factors may result in sufficient short wave radiation throughout the cloud to induce small grains to radiate detectable 12 μm emission from most of the cloud projected area.

Comparison of dust column density, calculated with the two component model of Boulanger et al. (1988), with the ^{13}CO images, fails to produce physically reasonable maps of the distribution of dust in cold portions of molecular clouds. The temperature distributions computed with this model produce images in which the grain temperature decreases and the estimated column density of dust increases from the cloud interior to the cloud edges. Furthermore, the computed dust column density is very sensitive to small variations in the large grain temperature when this parameter is less than 20 K. A better estimate of the large grain spatial distribution are obtained by assuming that in cold regions the large grain temperature is roughly constant at about 18 K, independent of the 60–100 μm color ratio.

Reliable estimates of total dust content of clouds requires the use of submillimeter data, which can trace the bulk of the dust mass in clouds. Although *IRAS* images constrain the total luminosity of regions, they cannot be used to reliably estimate the cold dust content of molecular clouds. Since we are unable to distinguish the warmer atomic regions, where the large grains radiate more readily, from the colder molecular clouds from the *IRAS* data alone, we are forced to conclude that *IRAS* maps are not useful tracers of the molecular gas, except insofar as this component is associated with luminous young stars which induce large grains to reveal themselves.

5.2. *Dust Emission and* ^{12}CO

In the context of the LGM, when we compare the ^{12}CO emission to the dust properties, different correlations emerge: (1) In low-luminosity regions, the dust temperature is a complex function of the ^{12}CO peak temperature. As the ^{12}CO peak temperature is increased, the dust temperature first decreases, and then, above a ^{12}CO peak temperature of roughly 15 K, it levels off and, in some regions, rises slightly (see Figs. 4 and 5). (2) In the low-luminosity regions, the dust opacity correlates better with the peak ^{12}CO temperature than with the integrated CO line emission. (3) In high-luminosity regions, the infrared intensities and opacities correlate better with the integrated ^{12}CO emission than ^{13}CO emission where the ^{12}CO peak temperature is in the range 20–50 K (see Fig. 7 for an example). These three properties may result from the contribution of ^{12}CO and dust emission in the externally heated boundary layers of clouds, especially in regions exposed to strong UV radiation. Further analysis of these relationships requires a detailed model of the transfer of radiation through a multicomponent dust cloud which takes into account gradients in the dust temperature along the line of sight (Xie, Goldsmith, & Zhou 1991).

5.3. *Dust Rings Surrounding* H II *Regions*

The *IRAS* images show that many bright H II regions are surrounded by complete or nearly complete rings of dust emission, even though no molecular tracer shows this morphology. The best examples of complete rings surround M42 and NGC 1977 in the Orion A cloud. A much larger ring surrounds the λ-Orionis region, and some partial shells are located to the west of the center of the Orion OB I association, as can be seen in Figure 1. Most of these rings cannot, or may only partially, be traced in CO or other molecular emission.

The gas lying immediately outside an H II region is exposed to intense levels of UV continuum and Lyα line radiation which can heat the dust to a temperature where most of the large grains radiate in the 60 and 100 μm *IRAS* band. Attenuation of the radiation field lowers the dust temperature and visibility of dust farther away, and dynamic effects may be responsible for the sharp inner edges of the rings. The expansion of the ionized gas, radiation pressure on the grains, and the evaporation of mantles may contribute to the removal of grains from the ring interiors. The rings appear more continuous in the dust than in the molecules since the dust is associated with both atomic and molecular phases.

5.4. *Implications for the Interpretation of Large Beam Infrared Measurements*

Although the brightest points in the infrared map are about 1000 times brighter than the average background, the ratio of total solid angle covered by the bright regions to that covered by the background is much less than one part per thousand. Only several hundred pixels out of about 200,000 have a dust-to-gas ratio close to the Draine & Lee value. Thus, the average IR characteristics of the Orion region are dominated by the

emission of the small grains in cold regions where only a few percent of the total dust associated with the molecular clouds is seen. The atomic region surrounding the molecular gas is more transparent to short-wavelength radiation, has a higher gas temperature (20–100 K), and has a higher dust temperature than that found in the fields dominated by molecular clouds.

If the correlations between 100 and 60 μm dust intensity and H I emission found for atomic gas (Boulanger & Perault 1988) are typical for H I gas in the Orion region, then about 10%–50% of the total dust content of the H I region radiates at 100 μm. In the LGM this corresponds to a derived $\tau(100\ \mu\text{m})/I(^{13}\text{CO})$ ratio between 10^{-4} and 5×10^{-4}. The position averaged mean value of the derived dust-to-gas ratio in Orion is 2×10^{-5}, close to that found in dark clouds. Thus, the 100 and 60 μm radiation of the entire Galaxy traces the H I phase more effectively than the H_2 phase. Furthermore, the derived average dust-to-gas ratio will be mostly representative of the conditions found in H I clouds. The relatively weaker infrared emission produced in the poorly irradiated interior portions of molecular clouds leads to a drastic underestimate of the importance of this component. Inspection of the *IRAS* emission from fields containing molecular clouds shows that although the clouds are visible, they do not stand out strongly against the background of emission associated with H I.

Particular care must be exercised in the interpretation of data from regions which have a different ratio of H I to H_2 than is present near the Sun, and where the star formation activity differs from what is typical in Orion. When the H_2/H I ratio increases, a greater fraction of the infrared emission will arise from cold, shielded regions in which the apparent dust-to-gas ratio is smaller than that in typical H I regions which dominate near the Sun. On the other hand, in hyperactive regions, such as the Galactic center, starburst galaxies such as NGC 6240, or in luminous dwarf galaxies, heated clouds near luminous sources may dominate the emission from cold clouds. These objects may be disproportionately bright with a large apparent dust-to-gas ratio and may resemble the luminous regions in Orion. Therefore, large variations in the infrared flux and the *IRAS* based dust-to-gas ratios are expected to be a function of the H I to H_2 mass ratio, the star formation activity, the shape of the initial mass function, and metallicity, all of which effect the production of radiation and its attenuation.

We thank C. A. Beichman, F. Boulanger, B. Draine, and J. L. Puget for useful discussions. We appreciate the effort of W. Rice, J. Good, and the IPAC staff to provide superior *IRAS* co-added data products. R. W. Wilson helped develop the algorithms used to analyze the data. This research was supported in part through the *IRAS* Guest Investigator Program by JPL-NASA grant No. 958479.

APPENDIX

We use the two component model of Boulanger et al. (1988) to analyze the infrared emission from the Orion region on a pixel-by-pixel basis. This model assumes that the infrared emission is produced by two distinct grain populations: (1) large grains whose temperature is close to thermal equilibrium with the ISRF, and (2) small grains whose temperature is higher and may be subject to stochastic, time-dependent variations due to the absorption of individual photons. These nonequilibrium grains make up a small percentage of the total grain mass, but in typical molecular clouds dominate the 12, 25, and 60 μm emission. In cold regions, where the large grain temperature is less than about 18 K, small grains may even dominate the 100 μm emission.

Boulanger & Perault (1988) find that, on average, about 45% of all the energy absorbed by dust is reradiated by small grains. Based on this result, and the assumption that the grain emissivity is proportional to frequency, Boulanger et al. (1988) present a plot (their Fig. 4) of the ratio of intensity in adjacent *IRAS* bands as a function of large grain temperature, which in turn depends on the energy density of the radiation field. We reproduce this plot in Figure 11, with the x- and y-axes reversed. Plotted this way, it is obvious that the large grain temperature is a multivalued function of $I(60)/I(100)$. Furthermore, since only the 12, 60, and 100 μm images can be used in the analysis (the 25 μm data has baseline and calibration uncertainties—see text), a two component model is the most complicated one which is fully constrained by these bands.

In our analysis, we are interested in recovering the large grain temperature from the observed ratio of fluxes in the 60 and 100 μm bands. In a two component grain model, a 60–100 μm flux ratio $0.2 < I(60)/I(100) < 0.7$ can be produced either by mostly warm large grains with a temperature in the range $18 < T_{lg} < 40$ K (the "upper branch" of Fig. 11), or by mostly small grains with $T_{lg} < 18$ K (the "lower branch"). However, if the small grains dominate, the 12 to 25, 25 to 60, and therefore the 12 to 60 μm flux ratio must be large. For the model of Boulanger et al. (1988), small grain emission produces $I(12)/I(60) > 0.41$.

Our analysis consists of a program which reads the 12, 60, and 100 μm images, and for each pixel forms two color ratios. The curve in Figure 11 is used to calculate the large grain temperature from $I(60)/I(100)$, using the ratio $I(12)/I(60)$ as a constraint. If the latter ratio is smaller than a critical value (0.41 in Fig. 4 of Boulanger et al.), the upper branch of the curve, corresponding to emission by warm large grains, is used. Where this threshold is exceeded, it is assumed that small grains dominate, and the lower branch of the curve is used. An image of the large grain temperature distribution is obtained, which, in conjunction with the 100 μm intensity image is used to compute the large grain 100 μm opacity using the method discussed in Langer et al. (1989).

The application of this method to *IRAS* data suffers several difficulties. First, the *IRAS* images have at least two kinds of imperfections which must be corrected. (1) The zero-point of the emission (the "baseline") must be found to eliminate the contribution offsets in the data due to both instrumental effects, gain variations, and the unavoidable contribution of background and foreground dust. (2) The *IRAS* images suffer from "striping" produced by the varying contribution of the zodiacal emission, and also introduced by the co-add image construction algorithms in the presence of bright sources. Even after "baselining," the raw intensity images are imperfect, and the resulting ratios exhibit clear signs of systematic error.

A second error results from the uncertainties of the two grain model. As discussed by Boulanger et al. (1988), there is strong evidence from color variations for systematic changes in the fraction of radiation absorbed by small versus large grains. In the model, this corresponds to variations in the threshold.

A third error is produced by the inevitable summation of the observed flux along the entire line of sight, which includes a variety of radiation fields, large and small grain mixtures, and large grain temperatures (see, e.g., Xie et al. 1991).

REFERENCES

Bally, J. 1989, in Structure and Dynamics of the Interstellar Medium, ed. G. Tenorio-Tagle, M. Moles, & J. Melnick (Heidelberg: Springer), 309
———. 1990, in Low Mass Star Formation and Pre-Main Sequence Objects, ed. B. Reipurth (ESO CP-33) (Garching-bei-München: ESO), 1
Bally, J., & Lada, C. J. 1983, ApJ, 265, 824
Bally, J., Langer, W. D., Wilson, A. A., & Stark, A. A. 1987a, ApJ, 312, L45
Bally, J., Stark, A. A., Wilson, R. W., & Henkel, C. 1987b, ApJ, 65, 13
Beichman, C. A., et al. 1986, *IRAS* Catalogs and Atlases: Explanatory Supplements (Washington: GPO)
Beichman, C. A., Wilson, R. W., Langer, W. D., & Goldsmith, P. F. 1988, ApJ, 332, L81
Bhat, Ch. L., Issa, M. R., Houston, B. P., Mayer, C. J., & Wolfendale, A. W. 1985, Nature, 314, 511
Bloemen, J. B. G. M., et al. 1986, A&A, 154, 25
Boisse, P. 1990, A&A, 228, 483
Boulanger, F., Beichman, C. A., Desert, F. X., Helou, G., Perault, M., & Ryter, C. 1988, ApJ, 332, 328
Boulanger, F., & Perault, M. 1988, ApJ, 330, 964
Castets, A., Duvert, G., Dutrey, A., Bally, J., Langer, W. D., & Wilson, R. W. 1990, A&A, 234, 469
Draine, B. T. 1990, in Interstellar Medium in Galaxies, ed. H. A. Thronson, Jr., & J. M. Shull (Dordrecht: Kluwer), 483
Draine, B. T., & Anderson, N. 1985, ApJ, 292, 494
Draine, B. T., & Lee, H. M. 1984, ApJ, 285, 89
Genzel, R. 1990, NATO ASI Chemistry in Space, ed. J. W. Greenberg (Dordrecht: Kluwer)
Genzel, R., Downes, D., Pauls, T., Wilson, T. L., & Bieging, J. 1979, A&A, 73, 253
Goudis, C. 1982, The Orion Complex: A Study of Interstellar Matter (Dordrecht: Reidel)
Graff, U. U., Genzel, R., Harris, A. I., Hills, R. E., Russell, A. P. G., & Stutzki, J. 1990, ApJ, 358, L49
Herbig, G. H. 1960, ApJS, 4, 337
Howe, J. E., Jaffe, D. T., Genzel, R., & Stacey, G. J. 1991, ApJ, 373, 158
Lada, E. A. 1989, Ph.D. thesis, Univ. Texas, Austin
Langer, W. D., Wilson, R. W., Goldsmith, P. F., & Beichman, C. A. 1989, ApJ, 337, 355
Levreault, R. M. 1988, ApJS, 67, 283
Malin, D. F. 1979, Mercury, 8, No. 4, 89
Mathis, J. S., Rumpl, W., & Nordsiek, K. H. 1977, A&A, 217, 425
McCaughrean, M. 1988, Ph.D. thesis, Univ. Edinburgh
Morgan, J. A., Schloerb, F. P., Snell, R. L., & Bally, J. 1991, ApJ, 376, 618
Mozurkewich, D., Schwartz, P. R., & Smith, H. A. 1986, ApJ, 311, 371
Press, W. H., Flannery, B. P., Teukolsky, S. A., & Vetterling, W. T. 1986, Numerical Recipes (Cambridge: Cambridge Univ. Press)
Puget, J. L., Leger, A., & Boulanger, F. 1985, A&A, 142, L19
Racine, R. 1968, AJ, 73, 233
Reipurth, B., & Bally, J. 1985, Nature, 329, 336
Sellgren, K. 1984, ApJ, 277, 623
Solomon, P. M., Rivolo, R., Barrett, J., & Yahill, A. 1987, ApJ, 319, 730
Thronson, H. A., Gatley, I., Harvey, P. M., Sellgren, K., & Werner, M. W. 1980, ApJ, 237, 66
Tielens, A. G. G. M., & Hollenbach, D. J. 1985, ApJ, 291, 722
Warren-Smith, R. F. 1983, MNRAS, 205, 349
Warren-Smith, R. F., Scarrott, S. M., King, D. J., Taylor, N. R., Bingham, R. G., & Murdin, P. 1980, MNRAS, 192, 339
Wolf, G., Lada, C. J., & Bally, J. 1990, AJ, 100, 1892
Xie, T., Goldsmith, P. F., & Zhou, W. 1991, ApJ, 371, L81